Utrecht University

Master thesis

Particle growth of iron oxide nanoparticles on SiO_2 and TiO_2 supports

Dónal Liam van Uunen

supervised by
N.A. Krans MSc.
Prof. dr. ir. K.P. de Jong

Inorganic Chemistry and Catalysis
Debye Institute for Nanomaterials Science
Utrecht University

October 19, 2019

Abstract

The effect of the support material on particle growth of supported nanoparticles is not yet fully understood. In this research colloidal synthesis, followed by the attachment was used to prepare a well-defined model catalyst suited to investigate the growth of Fe/SiO_2 and Fe/TiO_2 during the Fischer-Tropsch to olefins (FTO) reaction. 7 nm iron oxide nanoparticles (Fe-NP) with a narrow particle size distribution were synthesized using the heating-up method and subsequently attached to SiO_2 and TiO_2 support materials. Despite the difference in Hamaker constants between SiO_2 and TiO_2, a similar Fe-loading per surface area was obtained. The catalytic performance in FTO was evaluated after activation in H_2 and CO. In general the activity of the supported Fe-NP was comparable to reference catalysts prepared by impregnation, however Fe-NP/P25 was less active. TEM and STEM analysis of the used catalyst revealed tremendous particle growth of up to 100 nm for Fe-NP/TiO_2 while SiO_2 supported Fe-NP remained stable after 100h on stream. Further experiment showed that growth already occurs during the activation in H_2 at temperatures above 325°C. A semi-quantitative EDX analysis revealed the presence of large amount ($\approx$ 80%) iron species on the TiO_2 support. Additionally, Mössbauer spectroscopy results indicated the presence of amorphous Fe_3TiO_3 or Fe^{2+} surface species for reduced Fe-NP/TiO_2. Base on these findings, a surface species assisted Ostwald ripening process was proposed as growth mechanism for TiO_2 supported Fe catalysts.

Contents

1. Introduction

The main building blocks for the chemical industry are ethylene, propylene and butylenes. These C_2-C_4 lower or light olefins belong to the most produced organic compounds around the world and are used in a large variety of intermediates and final products such as polymers, solvents and coatings. [1, 2] For instance, tremendous amounts of ethylene are required for the production of plastics such as polystyrene (PS), polyvinylchloride (PVC) and polyethylene terephthalate (PET). The primary method of production of most lower olefins is via steam cracking of crude oil. However, in the endeavour to develop more sustainable processes, the use of alternative feedstocks becomes increasingly important. As an alternative to oil, other carbon containing sources such as coal, biomass and natural gas can be used as a feedstock. These feedstocks must then first be converted into synthesis gas, a mixture of H_2, CO and possibly CO_2, which in turn can be used to produce olefins. This can be done indirectly, by first converting the synthesis gas to methanol using a $Cu/ZnO/Al_2O_3$ catalyst followed by the a methanol to olefins reaction over a zeolite [3, 4] or directly, in the Fischer-Tropsch to Olefins (FTO) reaction. [1] These reactions happen on the surface of the active phase, therefore maximizing the surface area by creating small particles will result more active catalyst compared to the bulk material.

In heterogeneous catalysis these small particles dispersed on a support material to provide stability. [5] However, due to the harsh activation and reaction environments particle growth can still occur. This will result in loss of active surface area and therefore a loss in activity. Two common growth mechanisms during catalysis are 1) Ostwald ripening, where relatively large and stable particles grow at the expense of smaller particles and 2) Coalescence, in this case whole particles meet after migrating over the surface and merge together to form one bigger particle. [6] Important factors for particle growth include the size and spatial distributions of the nanoparticles. Another factor that can drastically influence the particle growth of supported metal catalysts is the support material. For instance T.W. van Deelen et. al. hypothesized different particle growth mechanisms for silica and titania supported Co catalysts and N. Masoud et.al. observed growth of Au particles on a TiO_2 support, but to a lesser extent for Au nanoparticles on SiO_2. [7, 8] In-situ X-ray diffraction experiments also indicated particle growth for an Fe/TiO_2 Fischer-Tropsch catalyst. [9] To better investigate the growth of Fe particles during activation and FTO and the role of support material, in particular titania and silica, model systems required. Unfortunately, conventional preparation methods such as incipient wetness impregnation, deposition precipitation or ion-exchange have limited control over the particle size and spatial distribution, resulting in less ovious differences before and after growth. Colloidal preparation methods such as the hot-injection or heating-up method on the other hand allow synthesis of well-defined particles with a narrow size distribution. Moreover, the synthesis and attachment of the colloidal particles to the support material are separated, thereby avoiding the possible formation of iron titanates/silicates during conventional preparation methods. In this research colloidal iron oxide particles are synthesized with the heating-up method and attached to SiO_2 and TiO_2 support materials. This model catalyst is then used to investigate the growth of iron oxide nanoparticles during the FTO reaction and activation step by employing (scanning) transmission electron microscopy combined with energy dispersive x-ray spectroscopy and Mössbauer spectroscopy.

2. Theory

2.1 Colloidal Synthesis

To prepare a model catalyst that can be used to investiga particle growth, a narrow size distribution is desired. During conventional preparation methods such as incipient wetness impregnation or deposition precipitation the nanoparticles are formed from a metal precursor that is already in contact with the support material. The colloidal synthesis of (iron oxide) nanoparticles separates the formation of the particles and the attachment on the support. This allows for a great control of the size and the shape of the nanoparticles. [10–14] While the application of colloidal nanoparticles in industry is limited due to the high cost, challenging scale-up and the large amounts of waste generated, it is an excellent way to prepare a model catalyst. The colloidal synthesis used in this research is a bottom-up approach, however top-down approaches also exist. A typical bottom-up synthesis consists of the thermal decomposition of a metal precursor in an organic solvent in the presence of a stabilizing ligand. Upon decomposition of the metal precursor monomers are formed and stabilitzed by the ligands. The monomers then nucleate and then grow to form nanocrystals.

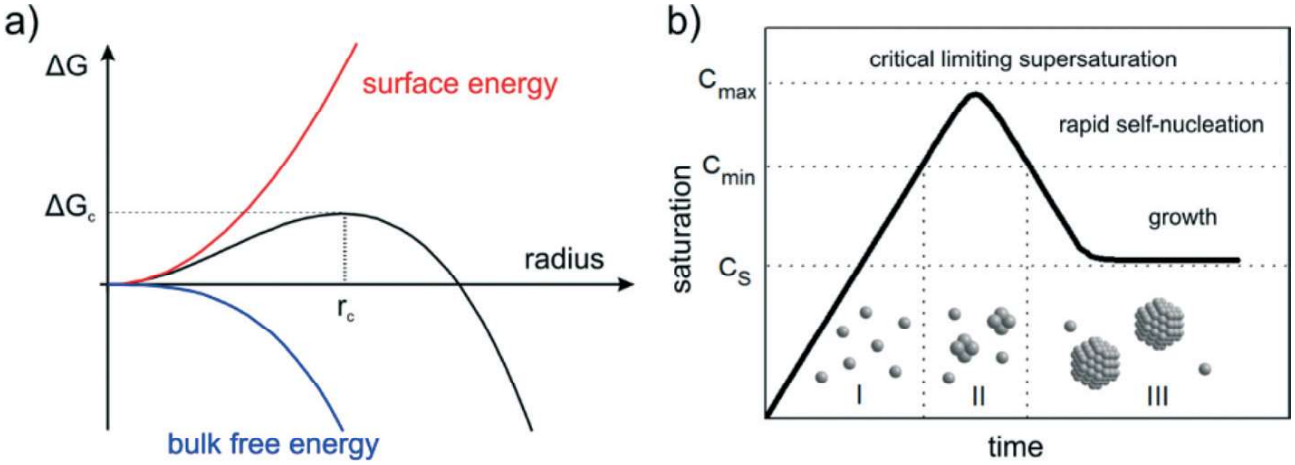

Figure 2.1: a) The free energy ΔG as a function the radius of the cluster, r. Below the critical cluster size rc, ΔG is positive and clusters are not stable. For clusters with a size larger than rc, *delta*G is negative and the particles are stable. **b)** The three stages of nucleation and growth as described by LaMer. (Reproduced from J. Polte. [15])

Around 1950 LaMer first described the model of nucleation and growth. [16] According to this model nanoparticles can only continue to grow if the nuclei reach a critical radius. Below this radius the clusters are not stable, due to the high surface energy. However, for particles larger than the critical radius the surface energy is compensated by the bulk free energy, see Figure 2.1a. The formation of particles can be divided in three stages as shown in Figure 2.1b In stage I the concentration of monomers builds up until it reaches a critical supersaturation. At this point nuclei can form and stage II begins. During the second stage, the nucleation will cause the concentration of monomers to drop until the concentration falls below the minimum concentration required for nucleation and no new nuclei can be formed. In the final stage III, the already existing nuclei can still grow, draining the leftover monomers from the solution. In order to prepare particles that are monodisperse, the separation of stage II and stage III is essential. There are two main synthesis methods that apply this seperation: Hot-injection and heating-up. In the first case, the solvent and stabilizing agents are heated to boiling point, then the iron precursor is injected quickly. Due to the sudden increase in concentration of monomers a burst of nucleation takes place, rapidly depleting the monomer concentration below the critical concentration for nucleation. New nuclei are now hard to form, but the existing nuclei can still grow, resulting in a uniform particle size. The second approach, the heating-up method, involves the addition of the precursor to a solution and then gradually heating the reaction mixture to and

above the decompisition temperature of the precursor. In contrast to the hot-injection method, the decomposition of the precursor proceeds relatively slowly while the temperature rises, however the high energy barrier for the homogeneous nucleation suppresses the nanocrystal formation until the supersaturation level is high enough. At this point burst nucleation is initiated similar to the hot injection method and nanocrystals with a narrow size distribution start to grow. [17, 18]

2.1.1 Precursors, ligands and solvents

For the colloidal synthesis a high boiling point solvent and ligands are used. Commonly used precursors for the synthesis of colloidal iron nanoparticles are iron pentacarbonyl ($Fe(CO)_5$) and iron(III) acetylacetonate ($Fe(acac)_3$), because they have approachable decomposition temperatures of 120°C and 200°C respectively. The advantage of $Fe(CO)_5$ is that CO is the only byproduct during decomposition. The decomposition reaction is quite complicated and multiple pathways are possible. [17, 18]. The other commonly used precursor, Iron(III) acetylacetonate is less toxic and does not decompose as quickly under ambient conditions, however it produces more by-products, often influencing the particle growth.

Ligands are present to stabilize the iron species and nuclei that are formed during the decomposition of the precursors. Oleic acid is often used as a ligand. It is a C18 carboxylic acid containing a double bond between C9 and C10. The metal precursor reacts with a carboxylic acid like oleic acid to generate an iron-oleate complex in situ. Jongnam Park et. al. proposed that dissociation of one oleate ligand by elimination of CO_2 between 200-240°C would trigger nucleation and the dissociation of the remaining ligands at 300°C causes the major part of the growth. [19] More recent thermogravimetric analysis (TGA) and differential scanning calorimetry (DSC) experiments reveal that the breakdown of the complex indeed starts around 250°C. [20] Knowing that the nanocrystals grow from the iron-oleate complex they reasoned that they could prepare the metal-surfactant complex with less expensive and toxic precursors. Instead of using iron pentacarbonyl, the complex was produced by reacting iron chloride ($FeCl_3 \cdot 6\,H_2O$) with sodium oleate. The complex was then heated in 1-octadecene containing oleic acid. This method allowed the preparation of iron nanocrystals on a 40-g scale. [19] Another alternative to iron pentacarbonyl or iron acetylacetonate is iron oxyhydroxide (FeOOH), also known as goethite. Ryan Hufschmid et. al. succeeded to form monodisperse particles up to 22 nm by the thermal decomposition of the goethite in the presence of oleic acid. [20]

Besides oleic acid, oleyl amine is often added as a ligand. This hydrocarbon is similar to oleic acid, but with an amine group instead of a carboxylic acid. It is added because the amine group can react with the carboxylic acid of oleic acid to produce water. The presence of water will initiate the formation of iron oxide and acts as a source of oxygen in the inert synthesis environment. A high boiling point solvent is used, because the mixtures need to be heated above the decomposition temperature of the iron precursors. Examples of solvents that can be used are 1-hexadecene (b.p. 274°C), octyl ether (b.p. 287°C), 1-octadecene (b.p. 317°C), 1-eicosene (b.p. 330°C) and trioctylamine (b.p. 365°C). The choice of solvent is important as this also affects the particle size. The reactivity of the iron-oleate complex increases with the boiling point of the solvent, therefore larger nanocrystals are produced in solvents with a higher boiling point. [19, 21]

2.2 Fischer Tropsch Synthesis (FTS)

2.2.1 Synthesis gas

In order to produce lower olefins from alternative feedstocks such as coal, biomass and natural gas instead of crude oil, these feedstocks must first be converted to synthesis gas (syngas). To produce synthesis gas from coal a process called gasification is used. The carbon in coal is converted to CO by partial oxidation (Equation 2.1) and to CO and H_2 via the steam reforming reaction (equation 2.2). Unfortunately, this process generates a large amount of excess CO_2 and the syngas derived from coal contains relatively high amounts of carbon monoxide, due to the low H/C-ratio of coal. [3] If necessary the H_2/CO-ratio of the synthesis gas can be adjusted by the water gas shift (WGS) reaction (Equation 2.3). [22] Alternatively, H_2 from another source can be added to increase the hydrogen content.

$$2\,C + O_2(g) \rightarrow 2\,CO(g) \qquad \Delta H = -221\ kJ/mol \tag{2.1}$$

$$C + H_2O(g) \rightarrow CO(g) + H_2(g) \qquad \Delta H = +131.3\ kJ/mol \tag{2.2}$$

$$CO(g) + H_2O(g) \rightarrow CO_2 + H_2(g) \qquad \Delta H = -41.2\ kJ/mol \tag{2.3}$$

A second potential carbon source is biomass. Biomass can be subjected to pyrolysis to increase the energy density prior to gasification. Like coal gasification, the carbon is converted to CO-rich syngas and the H_2/CO-ratio might need to be adjusted for further transformations. Syngas derived from coal and biomass suffer from contaminants such as sulphur that are potentially poisonous to the catalysts used in syngas processes and therefore requires purification. Another alternative feedstock is natural gas. The major component of natural gas is methane (CH_4) and is widely used to generate syngas. Three possible processes for the conversion of natural gas to syngas are: steam reforming (Equation 2.4), partial oxidation (Equation 2.5) and auto thermal reforming (a combination of the first two methods). The most used process is steam reforming yielding H_2-rich synthesis gas ($H_2/CO = 3$). The composition of the gas can then be adjusted by a reverse WGS reaction (Equation 2.6). Partial oxidation of CH_4 [22] produces a H_2/CO ratio of 2/1 directly, however the catalyst used in these processes deactivates faster than with steam reforming, due to a larger amount carbon deposition under the conditions required for the partial oxidation. [23–25]

$$CH_4 + H_2O \rightarrow CO + 3\,H_2 \qquad \Delta H = +206.1 kJ/mol \tag{2.4}$$

$$2\,CH_4 + O_2 \rightarrow 2\,CO + 4\,H_2 \qquad \Delta H = -71.4\ kJ/mol \tag{2.5}$$

$$CO_2 + H_2 \rightarrow CO + H_2O \qquad \Delta H = +41.2\ kJ/mol \tag{2.6}$$

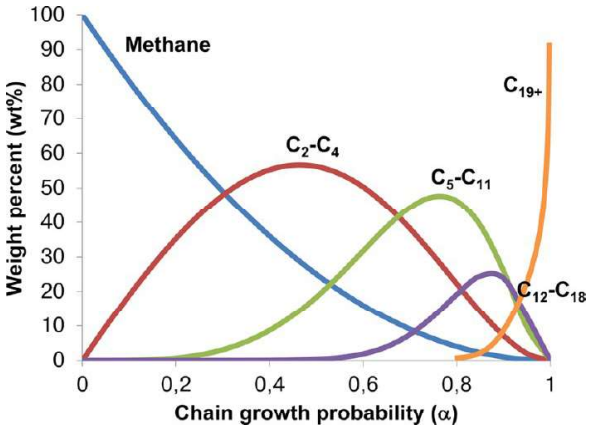

Figure 2.2: The product distribution in wt.% of hydrocarbons with n carbon atoms as a function of the chain growth probability α according to the Anderson-Schulz-Flory model. Image is obtained from H.M.Torres Galvis et. al. [26]

2.2.2 Product distribution

Synthesis gas can be converted to hydrocarbons using Fischer-Tropsch synthesis (FTS). The general equation for the conversion of synthesis gas to alkanes or alkenes is given by Equation 2.7. A range of products with different hydrocarbon chain lengths can be formed. The length of the hydrocarbon chains is dependent on the reaction conditions, the type of catalyst used and the presence of promoters. These factors influence the so called chain growth probability α. The Anderson-Schulz-Flory models described the product distribution depending on the value of the chain growth probability, see Figure 2.2. Lower chain growth probabilities will lead to smaller hydrocarbons, like methane or light olefins (C2-C4), while higher chain growth probabilities will result in heavy hydrocarbon chains (C5+). [1]

$$n\mathrm{CO} + 2n(+2)\mathrm{H_2} \rightarrow \mathrm{C}_n\mathrm{H}_{2n(+2)} + n\mathrm{H_2O} \tag{2.7}$$

2.2.3 Active phase

Active metals for Fischer-Tropsch synthesis are iron, cobalt, nickel and ruthenium. Nickel has a high selectivity to methane which is unfavourable and also produces volatile carbonyls at FT reaction conditions. Ruthenium is highly active, but the high cost of the metal limits the use for industrial scale applications. [1] Iron and cobalt are therefore the most promising candidates for Fischer-Tropsch synthesis. Cobalt is typically used for the production of waxes and middle distillates in the low temperature Fischer-Tropsch (LTFT) synthesis, which takes place at temperatures between 220-240°C. [10] Higher temperature will cause the selectivity of the cobalt catalyst towards methane to increase rapidly as the chain growth probability α to shifts to lower values for higher temperatures. Iron on the other hand can also operate at higher temperatures (220-350°C) producing light olefins and is therefore an excellent choice for Fischer-Tropsch to Olefins (FTO). Another benefit is that unlike cobalt, iron-based catalyst can be used for synthesis gas with a lower H_2/CO ratio. This is particularly interesting for the use of the CO-rich syngas derived from biomass or coal as no additional step is required to adjust the H_2/CO ratio.

Iron catalyst generally need activation before proceeding in the FTO reaction. First the catalyst is reduced in H_2 followed by a carburization step in H_2 and CO. This is necessary, because the active phases in FTO are thought to be α-Fe and iron carbides. Some iron carbide phases that could be formed during the activation or FTS/FTO are ϵ-Fe_2C, ϵ-$Fe_{2.2}C$, Fe_7C_3, χ-Fe_5C_2, θ-Fe_3C. From this selection χ-Fe_5C_2 and ϵ-Fe_2C are typically considered the most active species, while θ-Fe_3C is (almost) inactive. [27]. Recent research showed that the Fe_7C_3 phase is also active and can even have a higher intrinsic TOF than χ-Fe_5C_2 and ϵ-Fe_2C. Not only the activity but also the selectivity can depend on the iron carbide phase; ϵ-Fe_2C is less selective towards methane and more selective to C5+ hydrocarbons compared to the other active iron carbides. [28].

2.2.4 Effect of the support material

Support materials can also greatly influence the iron phases that are formed and therefore affect the performance of the catalyst. K. Cheng et.al. found a higher degree of carbidization for Fe on carbon then Fe on silica, leading to a higher activity. [29, 30] In another study using Mössbauer spectroscopy, the amount of iron carbides formed on different supports was investigated. The spectral contribution of χ-Fe2.5C was the highest for ZrO_2 and CeO_2 supported catalyst, followed by catalysts with TiO_2 and SiO_2 as support material while the least amount of active phase was formed on γ-Al2O3. [31] Besides the amount and type of iron carbides formed, support materials can also have an effect on stability of the particles during the reaction. For instance T.W. van Deelen et. al. [7] hypothesized different growth mechanisms for SiO_2 and TiO_2 supported Co catalysts during FTS. Addtionally, in-situ X-ray diffraction experiments indicated particle growth for an Fe/TiO_2 Fischer-Tropsch catalyst. [9].
Previous research with colloidal iron oxide nanoparticles on pristine carbon nano tubes (CNT) produces a relatively stable catalyst that remained active over 100h in Fischer-Tropsch synthesis. [11, 32] However, attachment of these same particles to surface oxidized carbon nano tubes (CNT-Ox) resulted in a lower loading and a rapid decline in activity already in the first 20 h on stream. This difference was attributed to the weaker van der Waals interactions between the iron NP's and CNT-Ox compared to pristine CNT. [33]

2.3 Hamaker Constant

A conventional method to describe the magnitude of the van der Waals force between two surfaces is with the Hamaker constant. This constant depends on the properties of the two materials as well as the surrounding media. There are three types of interaction that contribute to the van der Waals force: The Keesom force; the interaction between two permanent dipoles and one induced dipole. The Debye force; the interaction between one permanent dipole and one induced dipole. The London or dispersion force; the interaction between two induced dipoles. These interactions result from the fluctuations in the electromagnetic field between two bodies. This can be referred to standing waves that occur at certain frequencies. [34] Lifshitz developed a theory to derive the so called Lifshitz-van der Waals constant from the optical properties of the materials. L.Bergström used this to obtain Hamaker constants for inorganic materials. The Hamaker constants for silica and titania in vacuum are 6.50 and 15.3×10^{-20} J respectively. The constant also depends on the medium, for instance in water the constant are calculated to be 0.46×10^{-20} J for SiO_2 and 5.35×10^{-20} J for TiO_2. [34] Due to this difference, the attachment of iron oxide nanoparticles to silica or titania is also expected to be different, which in turn could possibly lead to diverging catalytic properties.

2.4 Growth mechanisms of particles

The two main growth mechanisms for nanoparticles are Ostwald ripening and coalescence, see Figure 2.3. With Ostwald ripening relative large and stable particles grow even bigger at the expense of the smaller less stable particles. Ionic species can be liberated from the smaller particles and diffuse towards the larger particles. This effect is more pronounced in systems with a broad particle size distribution, so generally catalysts with a narrow particle size distribution are more stable. [6,35] The second process, coalescence, can occur when two particles migrate over the surface, meet each other and merge together to form a bigger particle. The rate of diffusion is dependent on the particle size and temperature. Smaller particles have a higher surface diffusion coefficient which also increases with temperature. [6]. Another important factor is the distance that the particles need to travel. A homogeneous spatial distribution maximizes the inter-particle distance, thereby reducing the chance for two particles to encounter each other and thus reducing the growth rate.

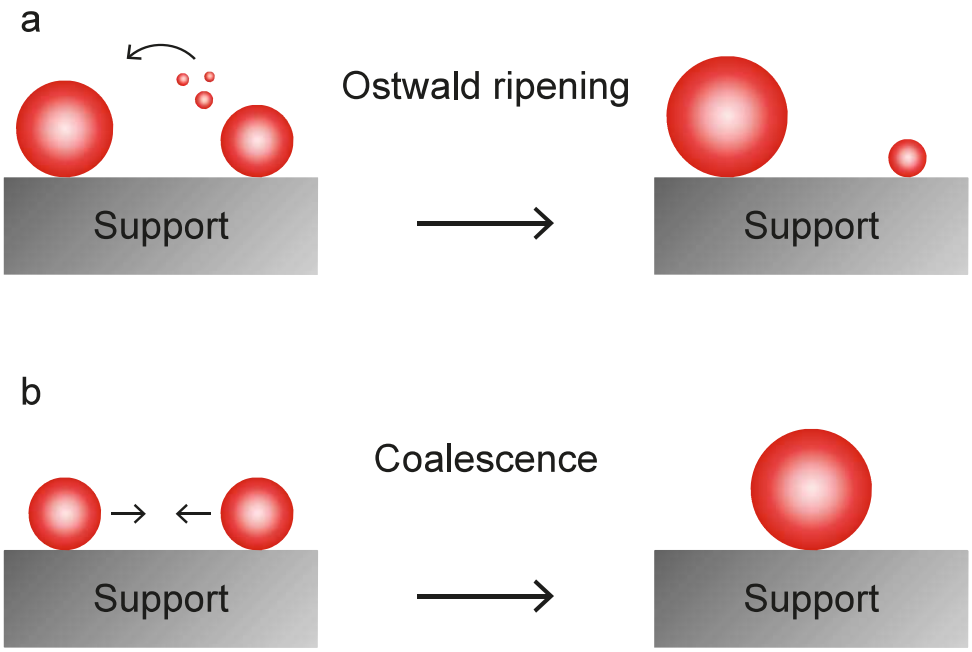

Figure 2.3: Schematic representations of the two main particle growth mechanisms: **a)** Ostwald ripening and **b)** Coalescence

2.5 Characterization techniques

2.5.1 Nitrogen physisorption

To obtain information of the pore structure nitrogen physisorption can be used. The N_2 pressure is slowly added at a constant temperature in the presence of the support of interest. N_2 molecules adsorb on the support trough Van der Waals interaction between the support and gas molecules. Increasing the amount of N_2 will lead to stacking of the molecules and multiple layers can be formed on surface. Eventually the rate of adsorption and desorption is equal and the system is in equilibrium. The pressure is then decreased and the release of the adsorbed N_2 can be measured. From the adsorption and desorption isotherms the surface can be calculated according to the model of Brunauer, Ememett and Teller (BET). An estimation of the particle size can be made from the BETsurface area using equation 2.8 where S is specific surface area in m^2/g and ρ is the theoretical density in g/cm^3. [36]

$$d_{BET} = \frac{6000}{\rho S} \tag{2.8}$$

2.5.2 X-ray diffraction

X-rays can be generated by accelerating electrons to high speeds and letting them collide with a metal such as Mo or Co. The released X-rays have a wavelength in the same order as the distance between planes in crystals. So when an X-ray beam is focused on a crystal a phenomena known as diffraction takes place. Braggs law relates the wavelength λ of the beam with the diffraction angle θ and the inter-planar distance d, see Equation 2.9. Constructive interference occurs if this equation is fulfilled. The intensity of the diffracted beam can be plotted as a function of the diffraction angle. These reflection can then be compared with reference patterns to identify the crystal phase in the sample.

$$2d \sin\theta = n\lambda \tag{2.9}$$

2.5.3 Transmission electron microscopy

The resolving power of a microscope is inversely proportional to the wavelength of the light used, see Equation 2.10 For visible light with a wavelength of 400 nm the resolution limit is around 200 nm. To circumvent the restriction of visible light on resolution, a beam with smaller wavelengths can be used. Luis de Broglie proposed that all particles have a wave function. The relation between the momentum and the wavelength of matter is given by $\lambda = h/p$. For electrons with a small rest mass this wavelength is in the order of 10^{-11}m (E = 1 keV). Such a small wavelength has a higher resolving power, hence using an electron microscope allows for greater magnifications than standard light microscopes.

$$R = \frac{0.61\lambda}{NA} \tag{2.10}$$

To investigate materials at a nanoscale, electrons are accelerated towards a cathode at high energies (200 kV). In light microscopes this beam is focused using optical lenses, but electrons cannot be focused this way. However, electrons carry charge and can therefore be focused on the sample using magnetic "lenses". A detector is present at the bottom of the microscope to collect the image. A schematic representation of an electron microscope and its components is shown in Figure 2.4.
In bright field transmission electron microscopy (BF-TEM) mode, the electrons that pass trough the sample are detected. Objects with a high density will allow less electrons to pass trough and will appear darker, while objects with lower density appear lighter as more electrons are detected. In scanning transmission electron microscopy (STEM) mode the beam is focused on a small area and is scanned along across a raster. For each point, a high angle annular dark field (HAADF) detector counts the electrons that are deflected. Heavier atoms (higher Z-value) will defect the beam more than

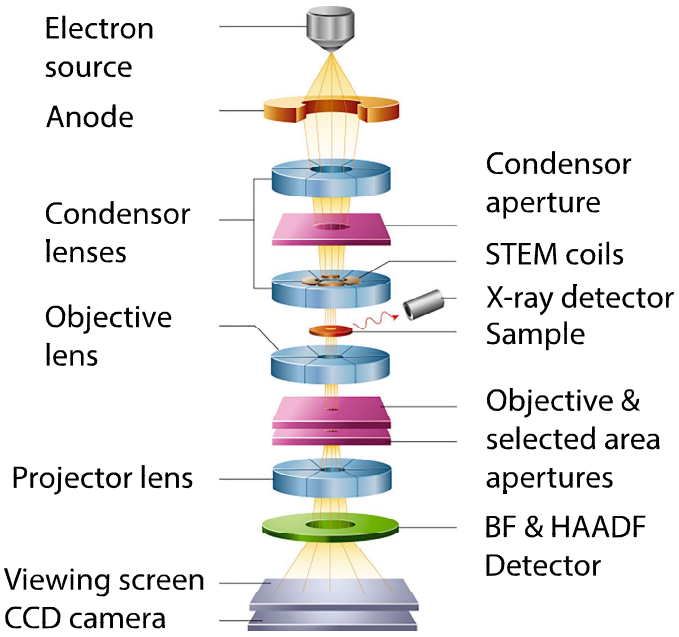

Figure 2.4: Schematic representation of a transmission electron and its components. Adapted from B.J. Inkson - Scanning electron microscopy (SEM) and transmission electron microscopy (TEM) for materials characterization. [37]

lighter atoms, resulting in more counts on the the annular detector. Areas containing high Z-value atoms will therefore appear brighter than areas with light or no atoms.

Additionally electron microscopes can be equipped with an energy dispersive X-ray detector (EDX). The electrons in the beam are accelerated to high enough energies that they can eject an electron from a core level of an atom, leaving behind an electron hole. An electron from an outer level will take its place and emit the surplus of energy as X-rays, see Figure 2.5. These emitted X-rays are characteristic and can be used to determine the presence of certain elements in a sample. The detection of energy dispersive X-rays can be combined with the STEM mode of the microscope. This way every pixel of the scanned area yields EDX spectrum. Every pixel can be colored based on the intensity of the signals originating from the element(s) of interest to produce a map of the element(s) of interest.

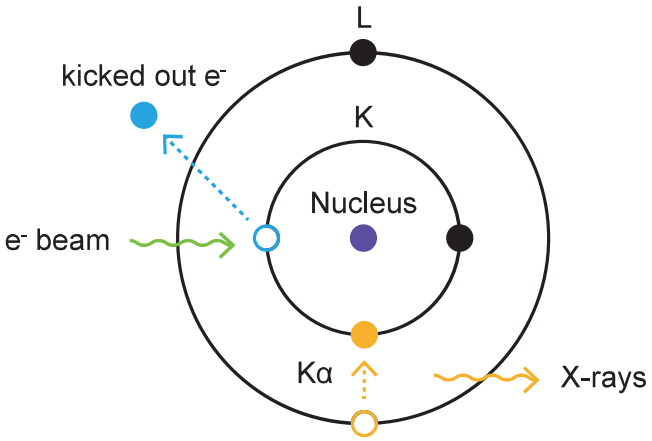

Figure 2.5: Schematic representation of the generation of X-rays in atoms exposed to a high energy electron beam.

2.5.4 Mössbauer spectroscopy

In general spectroscopy uses the electromagnetic radiation to probe different energy states of matter. In UV-VIS spectroscopy for instance, valence electrons electrons can undergo a transition from the ground state to the excited state by absorbing a photon. The system can return to its ground state by vibrational relaxation, emission of a photon or a combination of the previous (fluorescence). Similarly, a core electron can be excited to an empty state. The energy difference of this transition is larger and therefore requires photons of higher energy, in this case X-rays. Besides electronic transition, nuclear transitions are also possible. With Mössbauer spectroscopy nuclear states are probed using gamma rays. These transitions are element specific and are sensitive to changes in the environment of the nucleus, yielding information about the oxidation state and magnetic field.

Source

Unfortunately gamma rays are difficult to produce or to harness; natural sources include for instance thunderstorms, cosmic rays, pulsars, magnetars and quasars. More conveniently gamma rays are also produced during radioactive decay, commonly following another decay mode such as α / β decay or electron capture. Not all elements are suited to be investigated with Mössbauer spectroscopy, as an isotope is required that decays to the element of interest and emits gamma rays. Moreover the half-time of the initial decay should not be too long or too short, as this will result in too low intensities or a decay faster than the measurement time. Target isotopes that are frequently investigated with Mössbauer spectroscopy include ^{129}I, ^{119}Sn, ^{121}Sb and most commonly ^{57}Fe. The latter isotope of iron is relatively stable and has a natural occurrence of 2.1 atom %. [38] The radioactive isotope ^{57}Co can be used as a source for gamma rays which can be absorbed by a target material containing ^{57}Fe. This is possible, because ^{57}Co decays to ^{57}Fe by electron capture (Equation 2.11), where the proton-rich nucleus of the cobalt isotope absorbs an electron from the K-shell. The ^{57}Fe is formed in an excited state and reverts to the ground state by either directly emitting a gamma-rays of 136 keV or by first emitting a photon of 122 keV, followed by the emission of a gamma ray with 14.4 keV. Both the energy and the halflife (100 ns) of the latter state are well suited for Mössbauer spectroscopy on ^{57}Fe and can be used to excite the target material.

$$\mathrm{p} + \mathrm{e}^- \rightarrow \mathrm{n} + \mathrm{v_e} + \gamma\mathrm{-rays} \tag{2.11}$$

Mössbauer effect

However this is not trivial, the emission of gamma-rays upon transitioning from the excited state to the ground state causes recoil in the nucleus. This recoil reduces the energy of the gamma-rays. In the gas phase the energy is reduced to to such an extent that re-absorption by the target nucleus is no longer possible. Luckily, Mössbauer discovered that in solids recoil-free events are possible. Unlike in the gas phase, the recoil energy in solids is lost to phonons, allowing a non-zero probability that the entire crystal acts as recoiling body. In this case the energy loss is minimal and the nucleus can emit the gamma-ray almost recoil-free. [39, 40]

Doppler-effect

As stated before the nuclear transition energies are highly sensitive to the environment. A different environment of the source compared to the target nucleus can cause a small shift in the transition energy, resulting in a drastic change in the absorption. To probe all nuclei in different environments it would be favorable to scan through wavelengths similar to how a UV-Vis spectrum is obtained. However, the gamma-rays created by the radioactive sources have a narrow bandwidth and it is rather difficult to change energy of the transitions in such a way that a spectrum is created. Alternatively, the energy of the photons can be altered by making use of the Doppler effect. In a Mössbauer experiment the source is accelerated with a range of velocities, slightly altering the wavelengths of the initial gamma-rays.

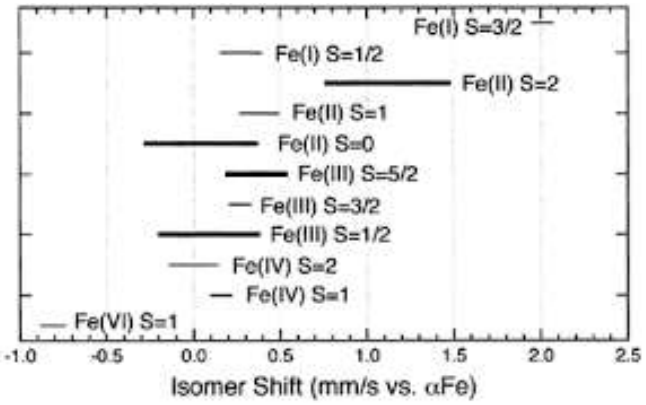

Figure 2.6: Possible isomer shift ranges for iron species with various oxidation and spin states. The image is obtained from B. Fultz 2011. [39]

Electric monopole interaction

The interaction between (for the most part) s- electrons and protons of the nucleus causes a shift of the whole spectrum. This is called the isomer or chemical shift and depends on the charge density of the s-electrons and yields information about the oxidation state and valancy. For example, Figure 2.6 shows possible isomer shifts for a range of iron species depending on their oxidation and spin state.

Electric quadrupole interaction

If a nuclear spin state has a spin greater than 1/2 it possesses a quadrupole moment. For instance the excited stateof ^{57}Fe of 14.4 keV as described in section 2.5.4 has a spin of 3/2 and therefore has a quadrupole moment. In a non homogeneous electric field at the nucleus, the state splits into two states with different magnetic spin quantum numbers. ($m_s = 3/2$ or $1/2$) resulting in a doublet in the Mössbauer spectrum. An inhomogeneous electric field is usually caused by the surrounding ions in a non-cubic symmetry or by the non-cubic symmetry of the electron density in the valence shell.

Magnetic dipole interaction

The interaction of the nucleus with a surrounding magnetic field can result in a splitting of the energy levels into $2I+1$ substates. This gives rise to 6 possible peaks for a 1/2 to 3/2 transition. The splitting is in the order of 10^{-7} keV and is therefore often referred to as hyperfine splitting. [39]

3. Experimental Methods

3.1 Catalyst preparation

3.1.1 Iron oxide nanoparticle synthesis

Iron nanoparticles of approximately 7 nm were synthesized according to the procedure described by Buonsanti et. al. [11, 41] A 100 ml three-neck roundbottom flask was filled with 1.2 mmol (0.35 g) hexadecanediol (Sigma-Aldrich, 90%), 0.75 mmol (0.21 g) oleylamine (Sigma-Aldrich, 70%), 0.43 g oleic acid (Sigma-Aldrich, 90%), and 10 mL 1-octadecene (Acros Organics, 90%). The flask was connected to a schlenk line via a reflux condenser. The remaining necks were closed with a septum. The mixture was heated to 120°C under stirring at 650 rpm with magnetic stir bar encapsulated in glass. The flask was slowly placed under vacuum and the contents were degassed for 30 min. 1 mmol (0.21 g) of $Fe(CO)_5$ (Sigma-Aldrich, ¿99.99%) was weighed in a glovebox and 1 ml octadecene was added to the vial. The three-neck roundbottomflask was flushed three times with nitrogen gas and allowed to cool to 90°C before injecting the $Fe(CO)_5$ solution trough the septum using a syringe. Subsequently, the reactants were heated to 290°C in 10 min. After heating for 1h the mixture was transferred to two vials and washed six times with isopropanol (VWR, technical grade). The iron oxide nanoparticles (Fe-NP) were centrifuged for 15 min at 2700 rpm and re-dispersed in a few drops of toluene (Acros Organics, 99.85%) after each washing step. After the final washing step the iron nanocrystals were dispersed in approximately 2 ml toluene.

3.1.2 Attachment of Fe-NP to Support

A similar Fe loading per support surface area obtained by varying the amount of support provided during the attachment. Depending on the support surface area, 200 - 800 mg of support was placed in a three-neck roundbottom flask. The amount of support used for each sample is listed in Table 3.1. (Most supports were purchased from Degussa-Evonik, except for silica C500-20 and titania B693-A-151 which were obtained from Engelhard.) 10 ml of octadecene was added to the previously synthesized iron oxide nanoparticles and then transferred to the flask with a pipet under stirring at 400 rpm. The system was placed under vacuum to remove the toluene and then further degassed at 120°C for 15 min. Next, the system was flushed three times with nitrogen gas and then heated to 200°C for 30 min. After cooling down the prepared catalyst was washed 6 times with hexane (Acros Organics 99%) : acetone (VWR, technical grade) $\approx 3:1$. After each washing step the suspension was centrifuged for 5 min at 2700 RPM, removing the supernatant. Finally the catalyst was dried subsequently for 1h at 60°C, 2h at 120°C and 3h under vacuum at 80°C. M. Casavola et. al. showed that the final drying step under vacuum is necessary to remove the remaining ligands from the colloidal synthesis. [11]

Table 3.1. Support material provided in the attachment of Fe-NP

Sample	Amount support used (mg)
Fe-NP/Aerosil Ox50-1	742
Fe-NP/Aerosil Ox50-2	742
Fe-NP/Aerosil Ox50-Mössbauer	757
Fe-NP/Aerosil 90	439
Fe-NP/Aerosil 130	275
Fe-NP/P25-1	798
Fe-NP/P25-2	799
Fe-NP/P25-Mössbauer	798
Fe-NP/P25-HL (High loading)	307
Fe-NP/P90	287

3.1.3 Incipient Wetness Impregnation

For comparison, silica and titania supported catalysts were also prepared via incipient wetness impregnation. 0.61 g of Aerosil Ox50 and 1.1 g of P25 was dried under vacuum at 80°C for 2h. The supports were subsequently impregnated under static vacuum and vigorous stirring with 0.25 ml (0.41 g) and 34 ml for Ox50 and P25 respectively of a 1.8 M $Fe(NO_3)_3 \cdot 9\,H_2O$ (Sigma-Aldrich, 98%), 16 µl HNO_3 solution. The impregnated supports were dried under vacuum over night at room temperature. Finally, the catalyst was calcined in static air for 2h at 350°C with a heating ramp of 5°C/min.

3.2 Catalytic performance and reduction experiments

3.2.1 High Pressure FTO

High pressure (10 bar) catalytic tests were performed on an Avantium Flowrence 16-port parallel fixed-bed reactor setup. 35 mg of prepared catalyst sieved to a grain size of 75-150 μg and 200 mg of SiC with a grain size of 212-425 μg were loaded in a steel reactor tube with a diameter of 2 mm. The catalyst were reduced and carburized in-situ prior to the FTO reaction. The reduction was performed with 33.3 ml/min hydrogen and 70 ml/min helium. (GHSV = 56800-81100 h^{-1}) at 350°C for 2h. The carburization step took place subsequently using a flow of CO/H_2 (90 and 42 ml/min respectively, GHSV = 72600 - 103700 h^{-1}) for 1h at 290°C. The catalytic performance was then evaluated at 300°C with the same gas flow as the carburization step over the course of 100h.
The product stream was analyzed with an online gas chromatograph(GC) equipped with a flame ionization detector (FID) and thermal conductivity detector (TCD). From the GC results the activity could be determined. Here we use the iron time yield (FTY) as a measure for the activity, which is based on the amount of moles of CO converted to hydrocarbons per gram of iron per second. The selectivity towards carbon products are determined by the amount of carbon atoms in the hydrocarbon products, excluding CO_2.

3.2.2 High Pressure reduction

High pressure reduction experiments were also performed on the Avantium Flowrence setup. Approximately 35 mg of prepared Fe-NP/P25 and Fe-NP/P90 sieved to a grain size of 75-150 μg and 200 mg of SiC with a grain size of 212-425 μg were loaded and reduced at 350°C for 2h in a flow of 90 ml/min and 42 ml/min H_2 and CO, respectively.(GHSV = 72600-103700 h^{-1}). No GC data was collected during the reduction.

3.2.3 Low Pressure FTO

For the evaluation of the catalytic performance at 1 bar, 20 mg of prepared catalyst sieved to a grain size of 75-150μg and 200 mg of SiC with a grain size of 212-425 μg were loaded into a tubular glass fixed-bed reactor. The catalyst in the low pressure setup were also reduced and carburized in-situ prior to the FTO reaction. The reduction took place for 2h at 350°C in a flow of 10 ml/min H_2 and 5 ml/min Ar. (GHSV = 14700 - 17600). The catalyst was then carburized in 3 ml/min H_2 and 3 ml/min CO = (GHSV = 5800-7100) at 290°C. FTO took place at 340°C in the same flow as the carburization. The product stream was analysed by an online GC equipped with a.

3.2.4 Low pressure reduction

To investigate the effect of the reduction step, 10-20 mg catalyst sieved to a grain size of 75 - 150 µm was mixed with 150 - 200 mg SiC (212 - 450 µm sieve fraction) and transferred to a tubular glass reactor. The catalyst was then reduced in a flow of 10 ml/min H_2 or CO and 5 ml/min Ar (GHSV = 7800-11700) for 2h at temperatures ranging from 240 to 400°C. Heating was done with a ramp of 5°C/ min.

3.2.5 Low pressure reduction in presence of water

Water vapor was introduced in the low pressure setup by connecting an unheated water reservoir in between the mass flow controllers and the glass reactor tube. Similar to the other reduction experiments 10-20 mg catalysts was sieved to a grain size of 75 - 150 µm and mixed with 150 - 200 mg SiC sieved to a grain size of 212 - 450 µm. The powders were then transferred to the tubular glass reactor and reduced in a flow of 10 ml/min H_2 and 5 ml/min Ar (GHSV = 7800-11700) for 2h at 300°C for Fe-NP/P25 and 350°C for Fe-NP/Ox50. Heating was done with a ramp of 5°C/min.

3.3 Characterization

3.3.1 (Scanning) transmission electron microscopy (TEM/STEM)

Synthesized Fe-NP and fresh, reduced and used catalyst were analyzed with a Thermo Scientific^{TM} Talos transmission electron microscope operated at 200 kV. The microscope is equipped with a high angle annular dark field detector (HAADF) for use scanning transmission electron microscopy mode (STEM) as well as an electron dispersive x-ray (EDX) detector. TEM samples of the synthesized Fe-NP were prepared by drop casting a diluted dispersion of the Fe-NP in toluene on a Formvar carbon 300 mesh grid. The catalyst powder of fresh, reduced and used samples were suspended in ethanol followed by ultra-sonication for 30 seconds to up to 2 min before drop-casting on a Lacey carbon grid. Particle size distributions were obtained from TEM micrographs by hand-counting $\approx$ 300 particles. STEM-EDX was employed for samples were Fe-NP could not easily be recognized, i.e. reduced or used catalysts that showed particle growth. In these cases the amount of particles counted for the size distributions was limited.

3.3.2 Identical location transmission electron microscopy

A sample for the identical location transmission electron microscopy (IL-TEM) experiment was prepared by drop casting an ultra-sonicated suspension of Fe-NP/P25 in ethanol on a SIMPore SN100-A50Q33 TEM grid. This grid contains 9 sockets with SiN windows of which the top-middle one is elongated. Using this elongated window as a guide, the location of catalyst particles could be mapped. This made the imaging of the same area before and after reduction in H_2 possible. After imaging the fresh catalyst, the entire chip was placed inside a pipet which was then inserted in a tubular glass reactor. The space between the pipet and the reactor was filled with some glass wool to direct the flow over the chip. The catalyst was reduced in H_2 with a gas flow and temperature program as described in the previous section.

3.3.3 Thermogravimetric analysis - mass spectrometry

To ensure that the drying steps after the attachment of the Fe nanoparticles to the support materials were sufficient to remove the ligands from the catalyst, thermogravimetric anyisis - mass spectrometry (TGA-MS) experiments were performed in a Perkin Elmer Pyris 1TGA instrument. The weight loss of approximately 8 mg of catalyst was measured while heating the catalyst from 30 to 700 °C (5°C/min) under a 16 mL min/min oxygen flow. Additionally, the evaporated components were analyzed with a mass spectrometer.

3.3.4 X-ray diffraction

X-ray diffraction (XRD) measurements were performed on a Bruker D2 phaser diffractometer with a fixed slit using Co-$K\alpha_1$ radiation with $\lambda = 1.78897$ Å. The measurements were taken at angles between 20°2θ and 80°2θ with an increment of 0.15°2θ and a scan speed of 0.8-1s/step. The crystallite sizes of the obtained nanoparticles were calculated from XRD line broadening analysis with k = 0.9 and an instrumental width of 0.1.

3.3.5 N_2-Physisorption

Nitrogen physisorption measurements were conducted at -196°C using a Micromeritics Tristar 3000 to study the pore structure and surface area of the support materials. The total pore volume was taken as the single point pore volume at $P/P_0 = 0.95$. The Brunaur-Emmett-Teller (BET) anaysis was also done at this point to obtain the BET surface area. From the BET surface area an estimation of the particle size (d_{BET}) was made.

3.3.6 Mössbauer spectroscopy

Transmission ^{57}Fe Mösssbauer spectra of Fe-NP/SiO_2-Mössbauer (3.9 wt.% and Fe-NP/TiO_2 (4.0 wt.%) were collected at 120 K with a sinusoidal velocity spectrometer using a ^{57}Co(Rh) source. Velocity calibration was carried out using an α-Fe foil at room temperature. The source and the absorbing samples were kept at the same temperature during the measurements. The Mössbauer spectra were fitted using the Mosswinn 4.0 program [Z. Klencsár, Nucl. Instr. Meth. B 129 (1997) 527]. The experiments were performed in a state-of-the-art high-pressure Mössbauer in-situ cell – developed at Reactor Institute Delft [Wezendonk et al., ACS Catal., 2016, 6 (5), pp 3236–3247]. The high-pressure beryllium windows used in this cell contain 0.08% Fe impurity whose spectral contribution was fitted and removed from the final spectra.

4. Results

In this research the growth of silica and titania supported iron catalysts was investigated using a colloidal model system. First, Fe-NP/SiO_2 and Fe-NP/TiO_2 model catalysts were prepared using colloidal synthesis followed by the attachment to support materials. Then catalytic performance during the FTO was evaluated and the used catalysts were analyzed. Finally, the particle growth of Fe-NP/SiO_2 and Fe-NP/TiO_2 was investigated with TEM, STEM-EDX and Mössbauer spectroscopy.

4.1 Preparation of SiO_2 and TiO_2 supported Fe-NP model catalysts

Before going into the particle growth of supported iron oxide nanoparticles (Fe-NP), it is important that the model systems with silica and titania supports are comparable. The preparation of the model catalysts involve the synthesis of colloidal iron nanoparticles followed by the attachment to the support materials. The attachment step could lead to dissimilar catalysts due to the difference in hamaker constants between SiO_2 and TiO_2 and/or differences in morphology and accessibility of the supports materials.

4.1.1 Support materials

In order to exclude the difference in the attachment to the support materials and the growth during FTO, the dissimilarities of the supports in terms of accessibility, morphology, particle size, available surface area and pore volume should be eliminated as much as possible. The approach here is to select a titania and a silica support where these parameters are similar. Promising support materials for the model catalysts were initially found by comparing known BET surface areas. For seven candidates the BET surface area, pore volume per gram, and pore diameter were determined by N_2-physisorption. The N_2 physisorption results are shown in table 4.1.

Table 4.1. Properties of silica and titania supports

Support	Type	BET surface area (m^2/g)	Pore volume (cm^3/g)	d_{BET} (nm)	d_{TEM} (nm)
Aerosil Ox50	SiO2	45.0	0.10	60.7	43.0 ± 25.0
Aerosil 90	SiO2	77.7	0.18	35.2	33.8 ± 24.1
Aerosil 130	SiO2	121.8	0.39	22.4	17.0 ± 10.2
Silica C500-20	SiO2	66.1	0.35	41.3	28.7 ± 11.4
P25	TiO2	41.8	0.15	37.5	21.2 ± 10.2
P90	TiO2	117.1	0.42	12.2	15.2 ± 8.2
B693-A-151	TiO2	45.8	0.22	30.9	24.6 ± 16.0

The surface area ranges from 45 to 120 m^2/g with pore volumes up to 40 cm^3. The particles size calculated with the BET is lower for supports with higher surfaces areas. Notably, the calculated particle size for silica support is larger than that for titania supports with roughly the same surface area e.g. Aerosil Ox50 and P25 both have a BET surface area of $\approx$ 40 m^2/g but a particle size of 60 and 37.5 nm respectively. TEM was also used to obtain the particle size of the support materials (Table 4.1). The particle sizes determined from TEM confirms the trend observed with d_{BET} however, in most cases the size determined by TEM is smaller. This could be caused by an underestimation of the surface area in N_2-physisorption as not all particles contribute the same to the surface area due to packing differences.
Additionally, TEM was used to examine the morphology of the support materials, see Figure 4.1) For supports of the same oxides, the morphology is similar. For example, all the silica supports contain spherical amorphous particles, of which some are relatively large. Also, some particles appear as if they are "melted" together. This appearance is observed more frequently for the supports with higher surface area (and smaller average particle sizes). In contrast to the silica supports, the titania

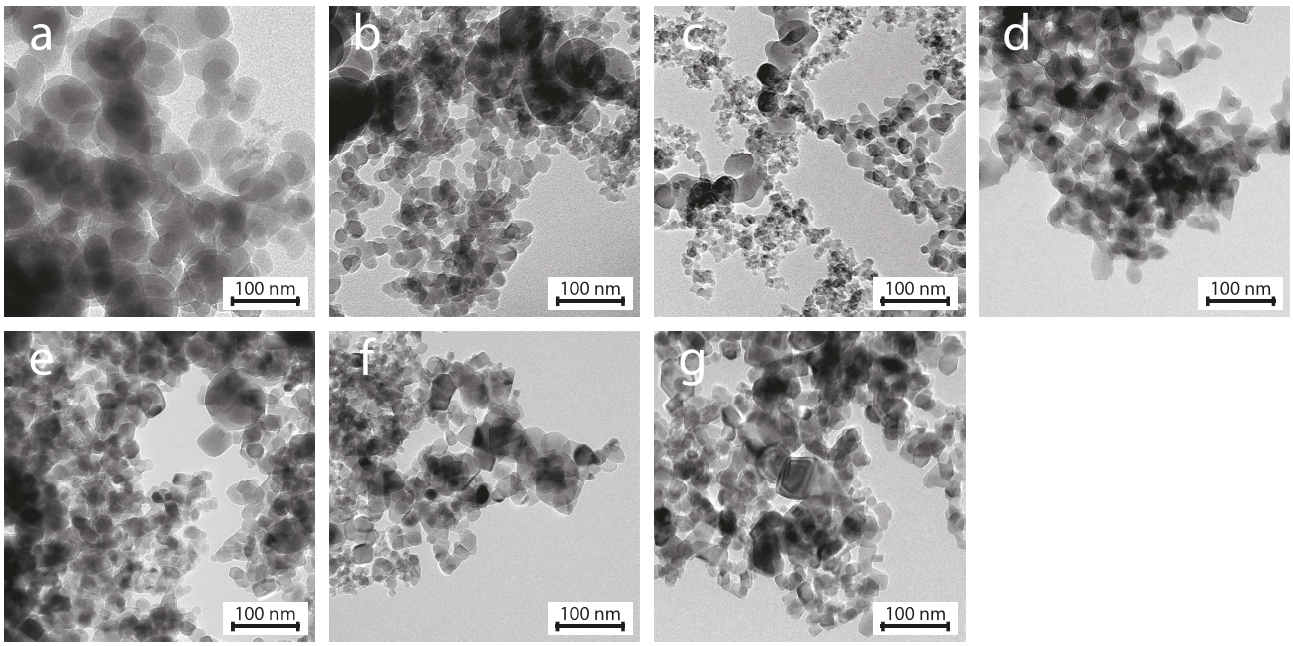

Figure 4.1: TEM images of the support materials: **a)** Silica Aerosil Ox50, **b)** Aerosil 90, **c)** Aerosil 130, **d)** SiO_2 C500-20, **e)** Titania P25, **f)** P90, **g)** TiO_2 B693-A-151.

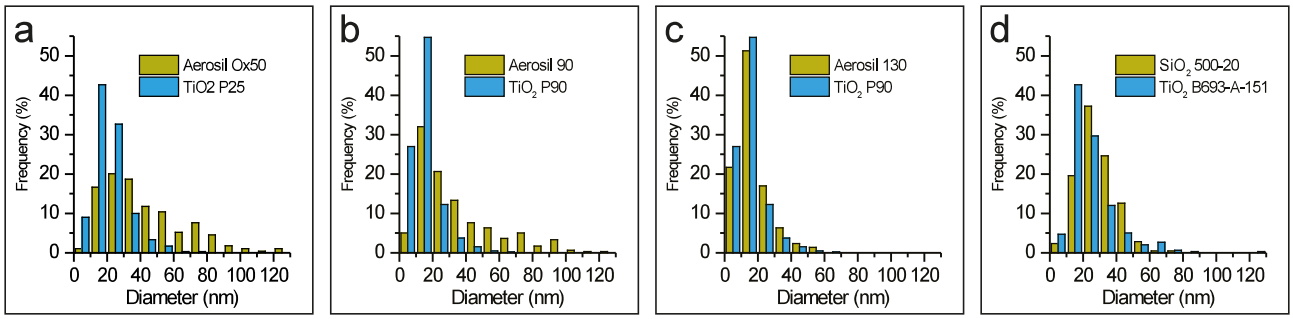

Figure 4.2: Particle size distribution as determined by TEM of possible combinations of silica and titania support. **a)** Aerosil Ox50 and P25, **b)** Aerosil 90 and P90, **c)** Aerosil 130 and P90 and **d)** SiO_2 C500-20 and TiO_2 B693-A151.

based support materials contain faceted particles which often results in square or rectangle-like shapes moreover, lattice fringes can often be observed. These observations indicate that the TiO_2 particles are crystalline, while the SiO_2 particles are amorphous. One possible combination of SiO_2 and TiO_2 materials suited for the model catalysts are Aerosil Ox50 and P25. Both materials have similar BET surface areas: 45.0 m^2/g for Ox50 and 41.8 m^2/g for P25 and also similar pore volumes (0.10 cm^3/g and 0.15 cm^3/g, respectively). The largest difference between these two supports is the particle size, where the average (TEM) particle size of Ox50 is twice as large as the P25 (43.0 nm and 21.2 nm respectively). The second combination of comparable materials is Aerosil 130 and P90, as the BET surface area and pore volume of these supports are very similar: 121.8 m^2/g and 0.39 cm^3/g for Aerosil 130 and 117.1 m^2/g and 0.42 cm^3/g for P90. Moreover, the difference in average particle size is only 1.8 nm. Besides the parameters displayed in tabel 4.1, the particle size distribution of the supports was taken into account. Figure 4.2 shows the particles size distributions of various combinations of SiO_2 an TiO_2 materials. Based on these particle size distribution a third possible combination could be considered; silica C500-20) and titania B693-A-151. These materials have extremely similar particle size distribution, however the BET surface area and pore volume are quite different from each other, making them less compatible. The most comparable supports materials were found to be: Ox50 & P25, Aerosil 130 & P90 and were selected. Fro practical reasons, the combination of Aerosil 90 & P90 was also investigated.

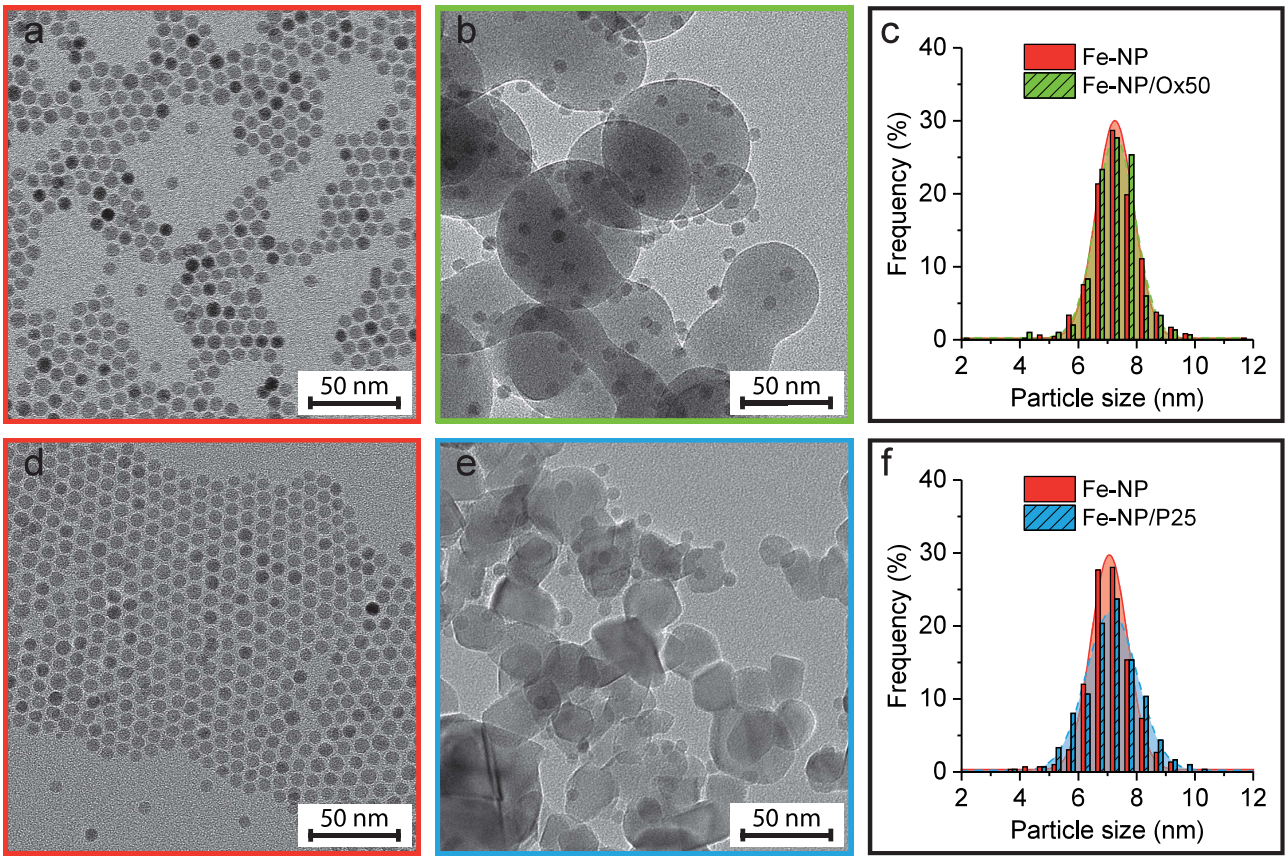

Figure 4.3: a,d) TEM of colloidal Fe-NP drop casted on a TEM grid. **b,d)** TEM images of Fe-NP attached to Aerosil Ox50 and P25 respectively and **c,f)** the obtained particle size distributions of the sytnhesized Fe-NP before and after attachment.

4.1.2 Iron oxide nanoparticle synthesis

Colloidal iron oxide nanoparticles were synthesized from $Fe(CO)_5$ using a heating-up method according to the procedure described by Buonsanti et. al. [41]. Figure 4.3a and 4.3d show representative images of iron oxide nanoparticles drop casted on a TEM grid. Note that the nanoparticles arrange in hexagonal structures upon drying, indicating that they are similar in size. The TEM images were used to determine the average particle size and distribution of the prepared nanoparticles, which are shown in Figure 4.3c and 4.3f. The synthesized colloidal Fe-NP have narrow size distributions; sample Fe-NP/P25-1 has an average particle size of 7.1 ± 0.8 nm which corresponds to a deviation of only 11 % and Fe-NP/Ox50-1 has a particle size of 7.3 ± 0.9 nm (12%). Table 4.2 shows the particle sizes of these and other synthesized particles as well as their particle size and after attachment to support materials.

4.1.3 Iron oxide nanoparticle attachment

Supported catalysts were obtained by attaching the prepared Fe-NP to the silica and titania supports. To compare the attachment of the Fe-NP on different supports, the amount of iron per available surface area of support was kept constant. Thus, depending on the surface area of the support, 200 - 800 mg of material was used for the attachment. For instance for Aerosil 90 with a surface area of 77.7 m^2/g only 439 mg was used, while for supports with the lowest surface area (Ox50 and P25) almost 800 mg was used. The as-synthesized iron nanoparticle dispersed in toluene were added to the support material together with octadecene and attached under inert atmosphere while heating and stirring. After washing and drying TEM images of prepared catalysts were obtained. (See Figure 4.3b and 4.3e). These images show that the iron nanoparticles were indeed attached to the supports, in most cases the particles are well dispersed, however in a few areas a less homogeneous distribution was observed. Interestingly, the particles attached to titania supports seem to attach preferentially

on the corners of the TiO_2 particles. Figure 4.3c and S1 show the particle size distributions of both the attached and unattached Fe-NP obtained from the TEM images. A gaussian fit is plotted through the bin centers as a visual aid. The particle size distribution of the Fe-NP after attachment is almost the same as prior to the attachment, indicating that the attachment procedure does not alter the Fe-NP significantly. However, a difference in the attachment of the Fe-NP between TiO_2- and SiO_2-supported catalyst was expected, due to the difference in Hamaker constants. A stronger or weaker interaction of the colloidal iron oxide particles with the support could have led to more or less orparticles attaching to the support material and thus a higher or lower Fe loading. ICP-analysis was performed to obtain the Fe loading of the supported Fe-NP as listed in Table 4.2. For the catalysts with lower surface area supports; Aerosil Ox50 and P25, the amount of iron is quite similar: 3.3 and 2.9 wt.%, respectively. This amount of iron present is also in agreement with previous results using the same synthesis methods for pristine carbon supports [11,33]. Also, for the combination Aerosil 130 and P90 (higher surface areas) the iron loadings are in the same range; 8.5 and 9.2 wt.%, respectively. Moreover, if we plot the Fe weight loading against the surface area of the supports determined by N_2-physisorption, it becomes clear that the amount of iron attached to the support materials depends predominantly on the amount of support material that is provided, as we aimed to keep the amount of iron per surface area constant. (See Figure 4.1.3a) The small differences can be explained by the variations from synthesis to synthesis such as the amount precursor ($Fe(CO)_5$) used.
To summarize, attachment of Fe-NP to support materials was successful. The size of the Fe-NP did did not change much during the attachment and model catalyst with similar particle sizes and weight loadings were obtained, thanks to the separation of growth and attachment made possible by the colloidal synthesis method. [11]

Table 4.2. Catalysts prepared by colloidal synthesis and attachment

Sample	d_{TEM} (nm)	d_{TEM} attached (nm)	Loading (wt.%)	BET surface area (m^2/g)
Fe-NP/Ox50-1	7.30 ± 0.90	7.3 ± 0.8	3.3	61
Fe-NP/Ox50-2	7.11 ± 0.71	7.2 ± 0.7	3.6	61
Fe-NP/P25 -1	7.11 ± 0.79	7.1 ± 1.0	2.9	38
Fe-NP/P25-2	8.03 ± 0.89	7.9 ± 1.1	3.7	38
Fe-NP/Aerosil 90	7.35 ± 0.66	7.4 ± 0.7	5.1	35
Fe-NP/P90	7.27 ± 0.82	7.0 ± 0.9	9.2	12
Fe-NP/Aerosil 130	7.52 ± 0.68	7.7 ± 0.8	8.5	22
Fe-NP/P90	7.26 ± 0.70	7.7 ± 1.8	3.4	12

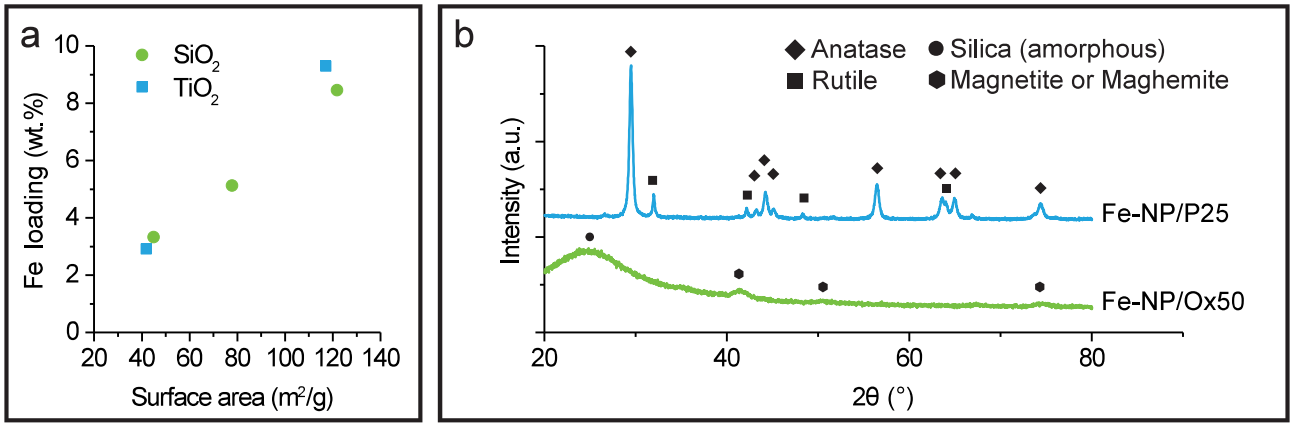

Figure 4.4: a) Iron weight loading plotted versus the surface area of the bare support material. Green circles indicate SiO_2 (Aerosil Ox50, Aerosil 90 and Aerosil 130) supported Fe-NP. Blue squares indicate TiO_2 (P25, P90) supported Fe-NP. **b)** X-ray diffraction pattern obtained for both Fe-NP/P25 (top) and Fe-NP/Ox50.

XRD

Powder X-ray diffraction was performed on the catalysts with Aerosil Ox50 and the P25 supports. The resulting diffraction patterns are shown in Figure 4.1.3b. For titania sharp peaks appear at several 2θ values, confirming the crystalline phase of titania. Titania is present in both the anatase and rutile phase indicated by for instance the peaks at 29.5 2θ and 32 2θ, respectively. The ratio of the anatase/rutile peaks is around 0.8, suggesting that the major phase of P25 is anatase. This is in accordance with a studie on P25. [42]. Other peaks corresponding to the anatase and rutile phases are indicated with symbols in Figure 4.1.3b. Unfortunately no clear iron or iron oxide peaks could be found for the titania supported Fe-NP, due to the overlapping peaks of the crystalline support. Unlike titania, the silica support material is amorphous, resulting in a broad peak observed around 24°2θ. Other small features are present for the Fe-NP/Ox50 originating from the iron nanoparticles. The peaks at 35 and 41.5 2θ indicate magnetite or maghemite structures [43], however due to the similar lattice parameters and the low intensity of the other peaks it is difficult to distinguish them.

Thermogravimetric Analysis-Mass Spectrometry (TGA-MS)

To ensure that the drying steps after the attachment of the Fe-NP to the support materials, TGA-MS was performed. In literature the peak at 55.55 is assigned to a decomposition product of oleic acid or oleyl amine. [11] In that report a small peak was observed for the carbon supported catalyst dried at 120°C, but after additional drying for 3h at 80°C under vacuum, no peak is present. This showed that the ligands that were still present after drying at 120°C are removed from the catalyst during the subsequent vacuum drying step. In our case, no peak at m/z = 55.55 was observed for both Fe-NP/SiO_2 and Fe-NP/TiO_2 dried at 120°C, see Figure 4.5. Also, after drying under vacuum at 80°C no decomposition products of the ligands were detected by the mass-spectrometer. The amount of ligands released from the TiO_2 supported catalyst could have been below the detection limit of the TGA-MS setup. Another interpretation is that the drying step at 120°C is already sufficient to remove the ligands from the catalyst. For both the samples dried at 120°C and those dried additionally under vacuum, the weight loss at 350°C (the expected temperature for the removal of ligands) is small compared to that of the carbon supported catalysts from M. Casavola. This observation leads to the conclusion that the used drying steps are indeed sufficient to remove most of the ligands for the SiO_2 and TiO_2 supported catalyst.

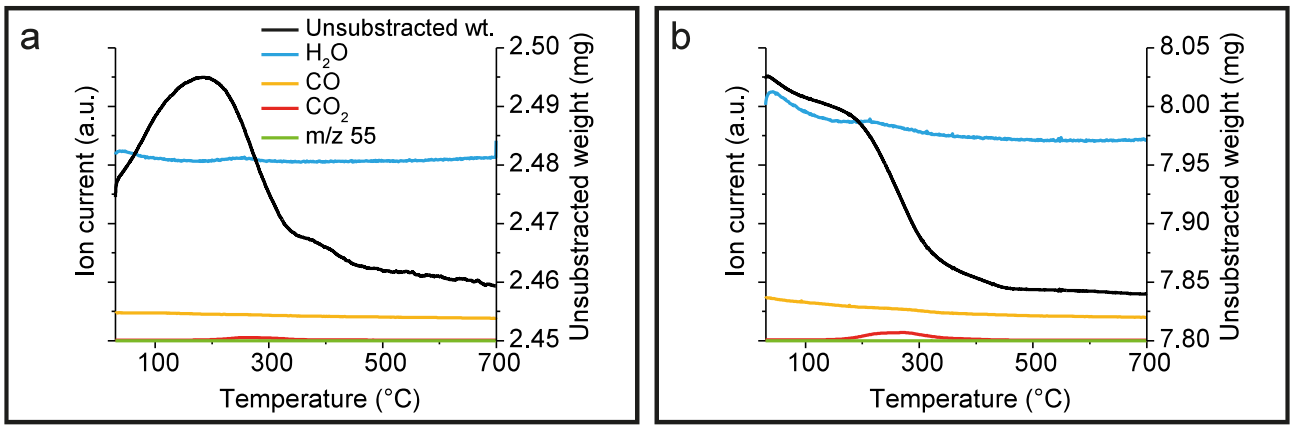

Figure 4.5: TGA-MS results of **a)** Fe-NP/Ox50 and **b)** Fe-NP/P25. The ion current of the mass spectrometer for different m/z values (left y-axis) and unsubstracted weight (right axis) are plotted against the temperature in °C.

4.1.4 Reference catalyst

Reference catalysts were prepared by impregnation of the Aerosil Ox50 and P25 supports with an $Fe(NO_3)_3$ solution under static vacuum, followed by a drying and a calcination step. (Impregnated samples are denoted i-Fe/Support.) The fresh impregnated catalyst were analyzed STEM-EDX as shown in Figure 4.6. The impregnated catalysts have a relatively inhomegenous spatial distribution and the particles are less defined than the catalyst prepared with the colloidal method. The average particle size for i-Fe/Ox50 is 33.7 ± 13.2 nm (n=70) and 12.5 ± 5.1 nm (n=82) for i-Fe/P25. The weight loading of the impregnated Ox50 and P25 catalysts were 3.8 and 3.4 wt.% respectively, as determined with ICP.

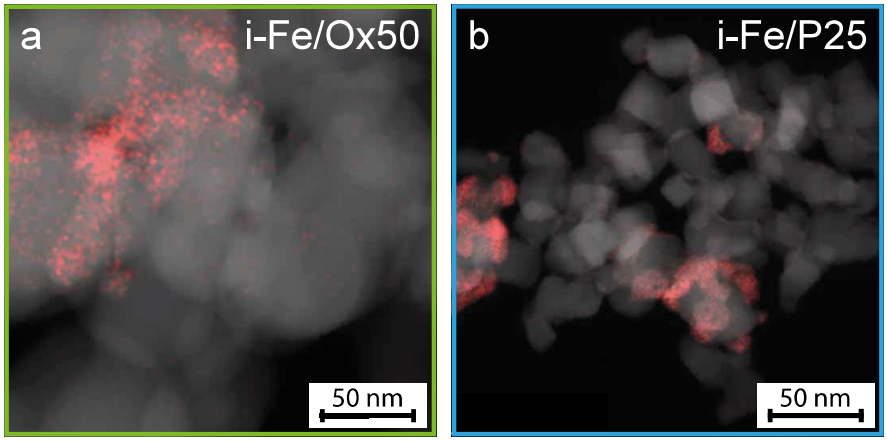

Figure 4.6: STEM-EDX maps of **a)** impregnated iron on Ox50 (i-Fe/Ox50) and **b)** impregnated iron on P25 (i-Fe/P25). While **a)** appears to made with a higher magnification, note that the average particle size of Aerosil Ox50 is larger than that of P25.

4.2 Catalytic performance

The performance of the supported iron oxide nanoparticles in the Fischer Tropsch to Olefins reaction was evaluated. The catalysts were placed in a Flowrence Avantium 16-port parallel fixed-bed reactor setup over the course of 100h under 10 bar pressure. The catalysts were reduced in H_2 for 2h and carburized for 1h in H_2/CO in-situ before reaching reaction conditions. The reduction and carburization temperature were 350°C and 240°C respectively. FTO took place at 300°C in H_2/CO. Figure 4.7 compares the activity in moles of CO converted per gram of iron per second, also called the Fe Time Yield (FTY), of the catalysts.

Table 4.3. Catlytic performance at t=100h

Catalyst	CO (%)	FTY (10^{-5} mmol CO/g Fe · s)	CH4 (%C)	C2-C4 Olefins (C%)	C2-C4 Paraffins (%C)	C5+ (%C)
Fe-NP/Ox50-1	5.6	9.9	49.0	27.8	12.5	10.8
i-Fe/Ox50	5.6	7.8	50.6	25.2	15.7	8.5
Fe-NP/P25-1	1.8	3.3	44.2	30.1	16.1	9.6
i-Fe/P25	5.3	7.8	38.0	24.6	19.2	18.1
Fe-NP/Aerosil 90	12.5	12.0	45.6	22.6	20.3	11.5
Fe-NP/Aerosil 130	15.0	9.3	44.8	25.4	18.1	11.8
Fe-NP/P90	16.4	9.7	40.6	19.5	22.7	17.2

There is difference in behavior of the impregnated and the colloidal prepared catalysts during the course of the reaction. At first the activity of the impregnated catalysts is higher than the supported Fe-NP, but the activity drops rapidly during the first 40 hours, eventually reaching similar conversion as their colloidal counterparts. Strikingly, the FTY of Fe-NP/P25-1 is significantly lower than all the

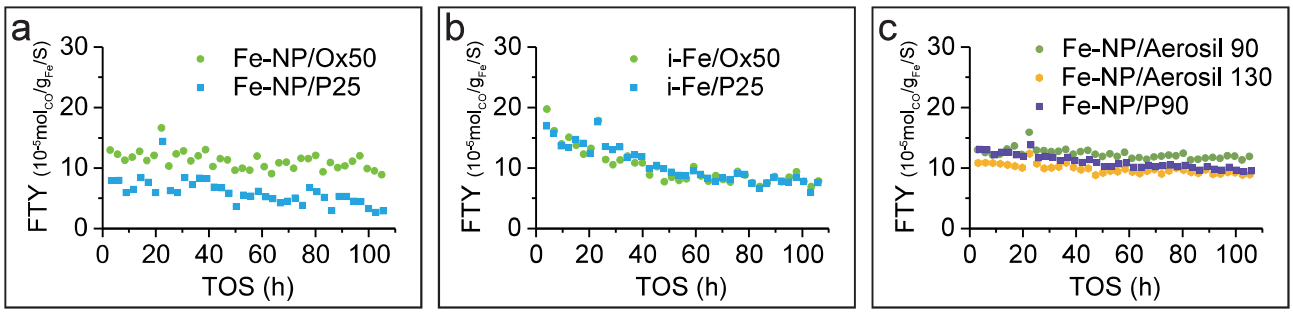

Figure 4.7: Catalytic activity during the FTO reaction performed under high pressure in the Flowrence Avantium 16-port parallel reactor setup. The figures show the FTY vs. time on stream (TOS) of **a** Fe-NP/OX50-1 (green circles) and Fe-NP/P25-1 (blue squares), **b)** i-Fe/Ox50 (green circles) and i-Fe/P25 (blue squares) and **c)** Fe-NP/Aerosil 90 (dark green circles), Fe-NP/Aerosil 130 (orange circles)and Fe-NP/P90 (purple squares).

other catalysts, including the impregnated catalysts with decreasing activity. On the other hand Fe-NP/P90 shows an FTY of 9.7 10^{-5} mmol CO/g Fe · s) which is comparable to that of Fe-NP/Aerosil 130 (9.3 10^{-5} mmol CO/g Fe · s).The activity of all catalysts as well as their selectivity towards methane, C2-C4 olefins/paraffins and hydrocarbons with more than 5 carbon atoms (C5+) after 100h on stream are listed in Table 4.3. (The selectivity vs TOS graphs are shown in Figure S2 provided in the supplementary information.) Generally, the titania supported catalysts show a slightly lower selectivity towards methane while the selectivity towards C5+ is higher with 18.1%C for i-Fe/P25 and 17.5 %C for Fe-NP/P90 as compared to 8.5%C and 11.5%C for i-Fe/Ox50 and Fe-NP/Aerosil 90, respectively. In contrast to the two mentioned titania supports, the selectivity towards C5+ of the less active Fe-NP/P25-1 is quite similar to the silica supported catalysts with only 9.6%C. The activity and selectivity towards methane, C2-C4 and C5+ for Fe-NP catalysts in the low pressure setup are plotted in Figure S3 in the supplementary information.

4.2.1 Used catalysts

After evaluating the catalytic performance in the FTO reaction, the used catalysts were analyzed by TEM. Figure 4.8a and Figure 4.8d shows TEM micrographs of the used Fe-NP/Ox50-1 and Fe-NP/P25-1 catalysts. The silica supported Fe-NP are still clearly visible and the particle size distribution (Figure 4.8c) obtained from the TEM images show that the particles retain their size even after the reaction. Surprisingly, for the used titania supported catalysts no particles were observed using bright- field TEM, while the 7 nm Fe-NP attached to the fresh catalyst could easily be recognized. (See Figure 4.3) Some larger core-shell particles were observed, but could not be designated as iron due to the small difference in contrast (density). To find out if there is still iron present and to pin-

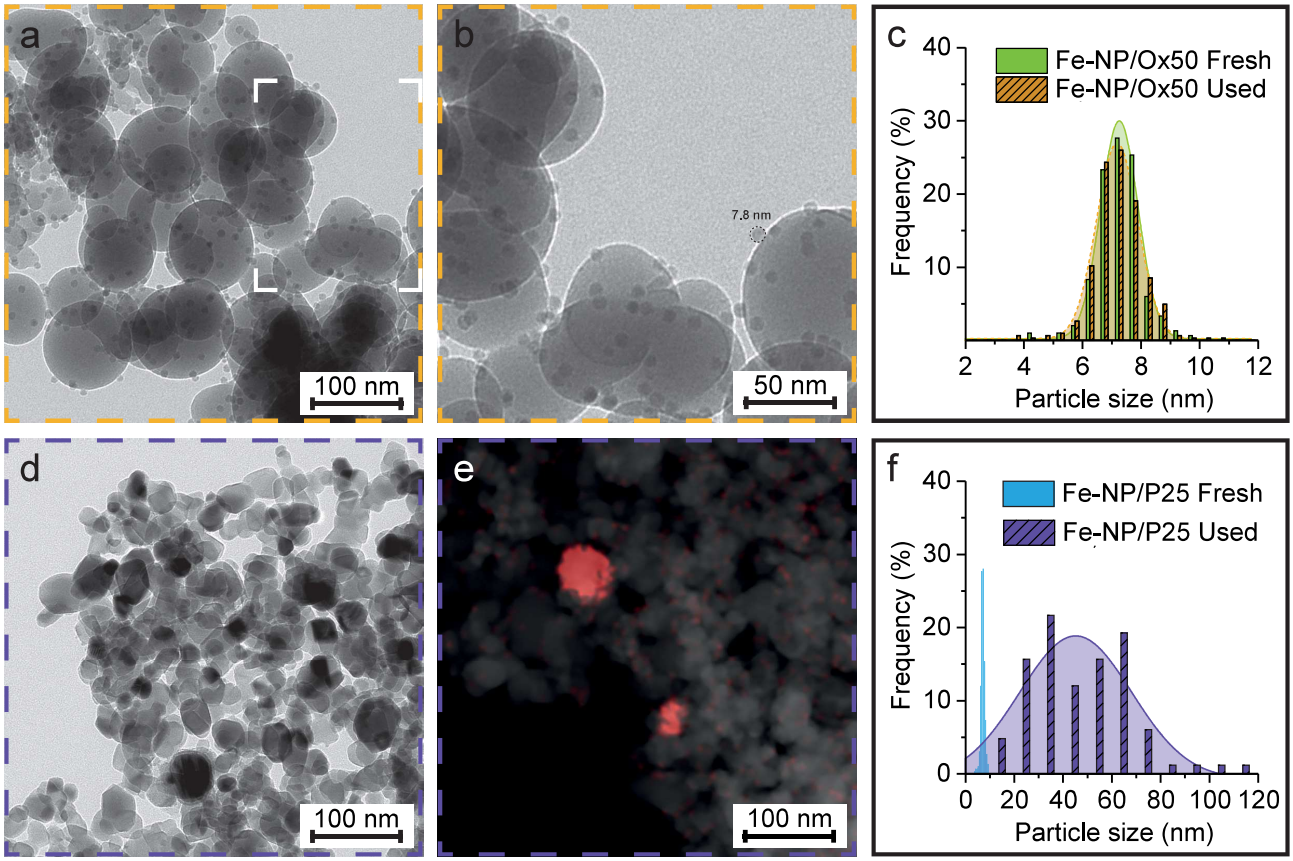

Figure 4.8: **a)** Bright field TEM image and **b)** magnification of the area indicated by white corners and **c)** particle size distribution of the used Fe-NP/Ox50 catalysts. **d)** Bright field TEM image, **e)** HAADF-STEM-EDX map and **f)** particle size distribution of the used Fe-NP/P90 catalysts.

point the location of the Fe-NP, HAAFD-STEM-EDX was used (Figure 4.8e). From this map we can conclude that there is still iron present, however the 7 nm particles that were attached to the titania support material have grown tremendously. A particle size distribution was obtained from several STEM-EDX images and compared with the size distribution of the fresh catalyst. Figure 4.8f clearly shows the change in size distribution after the reaction. Moreover, large particle were also detected for the other titania supported catalyst, Fe-NP/P90, while the Aerosil 90 and Aerosil 130 supported iron oxide nanoparticles show no growth. Similar results were found when analyzing used catalyst from the low pressure setup. The final particle size of the used catalyst is slightly smaller compared to the high pressure setup, but the Fe-NP still grow significantly to 36.1 $\pm$ 16.4 nm, see Figure S4 in the supplementary information. This discrepancy could have been caused by the higher H_2 flow of 90 ml/min in the high pressure setup, compared to only 3 ml/min in the low pressure setup.

4.3 Particle growth during the reduction step

The TEM and STEM-EDX images of the used catalyst showed that the Fe-NP with a titania support had grown substantially. The question arises at what point during the process the growth occurs, considering that three steps with distinct conditions are involved; 1) Reduction for 2h in H_2 at 350°C 2) Carbidization for 1h at 300°C in H_2/CO and 3) FTO for 100h at 300°C in H_2/CO. The first step, the reduction, occurs at the highest temperature. Therefore the influence of the reduction step was investigated first.

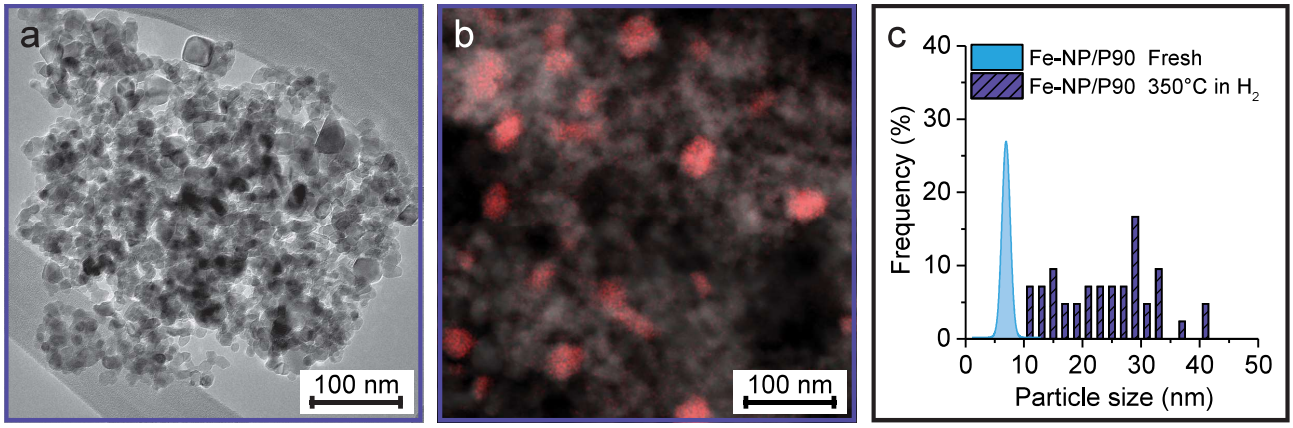

Figure 4.9: a) Bright field TEM image and **b)** STEM-EDX map of the reduced Fe-NP/P25-1 catalysts. **c)** Bright field TEM image, **d)** STEM-EDX map and **e)** particle size distribution of the reduced Fe-NP/P90 catalysts.

4.3.1 High pressure reduction

Approximately 20 mg of the P25, P90 supported catalyst were loaded in steel reactor tubes and reduced in the Flowrence under the same condition as the reduction step during the high pressure catalytic test. The reduced catalysts were analyzed with TEM as well as STEM-EDX. After the reduction in H_2 no particles were identifiable with TEM as shown in Figure 4.9a, similar to what was observed for the used catalyst (4.8). STEM-EDX maps revealed the presence and location of the iron oxide particles, see Figure 4.9b. It is evident that the iron oxide particles have grown significantly, indicating that particle growth already occurs during the reduction step. For the P90 supported catalyst a particle size distribution was obtained and compared with the distribution of the fresh catalyst as shown in Figure 4.9c. The distribution for the reduced Fe-NP/P90 catalyst is broadened with particle sizes up to 40 nm and an average particle size of 24.1 nm ± 8.2 nm. Unfortunately, no reliable particle size distribution could be determined for the P25 supported catalyst, because of the small amount of particles captured. However, STEM-EDX maps do confirm that particles also grow to up to 40 nm with P25 as support material. This is a smaller than the final particle size of the used Fe/P25 catalyst, where particles of up to 100 nm were found. Though, it should be taken into account that particles might continue to grow during the carbidiziation step or while under FTO conditions for 100h.

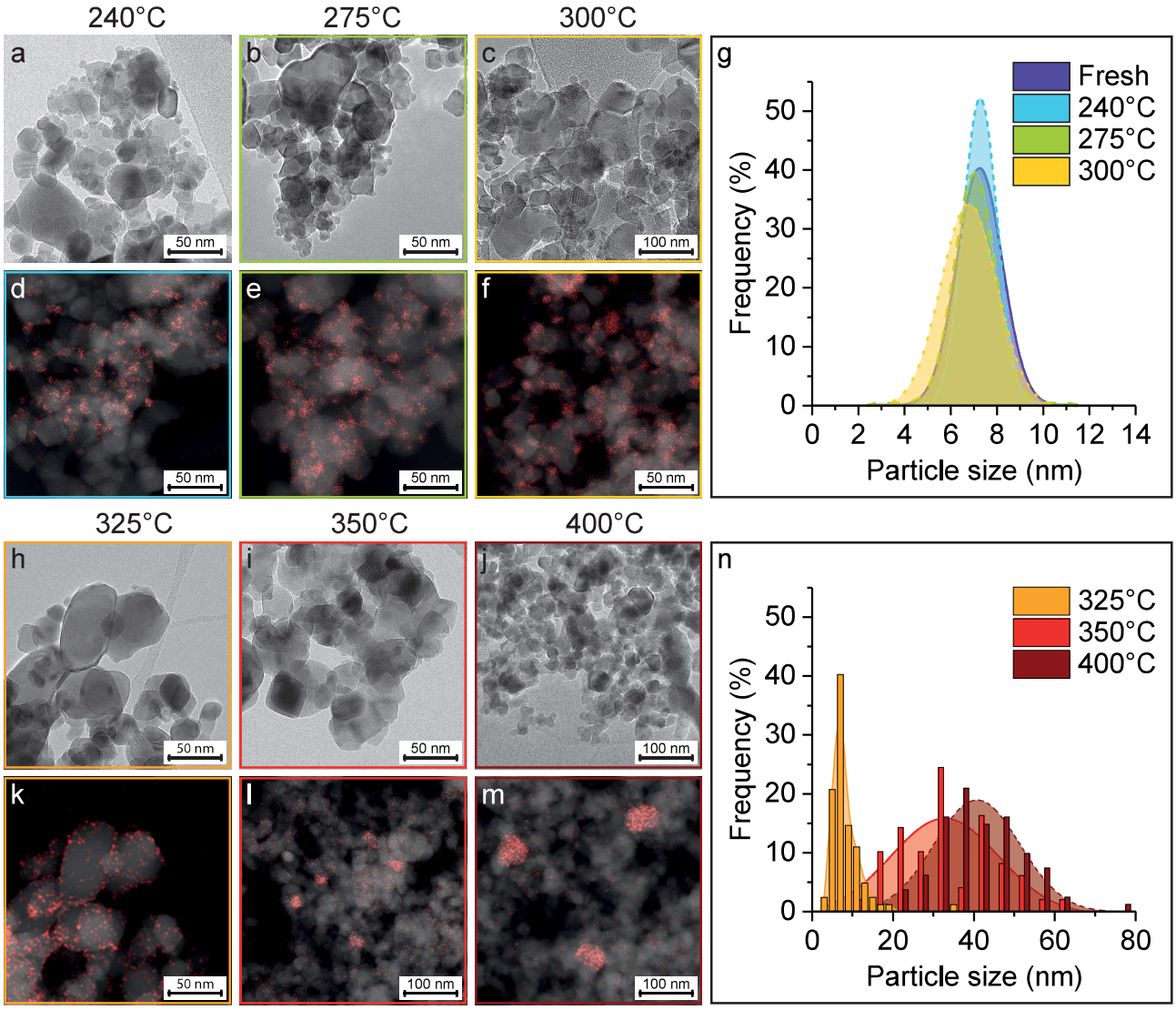

Figure 4.10: a,b,c) TEM image and **d-f)** HAADF-STEM-EDX maps of P25 supported catalysts reduced at 240, 275 and 300°C and **g)** a gaussian fit of the particle size distributions obtained from the TEM images. **h,i,j)** TEM images and **k,l,m)** STEM-EDX maps of the catalysts reduced at 325, 350 and 400°C and **n)** the particle size distribution obtained from the TEM/STEM-EDX images for the catalyst reduced at 325°C and from the EDX maps for the catalysts reduced at 350 and 400°C with gaussian fits.

4.3.2 Reduction temperature

The previous experiment showed that the reduction step is crucial for particle growth of the titania supported iron oxide nanoparticles. In this section the influence of the temperature on the growth behavior is investigated. Fe-NP/P25 (2.9 wt.%) were reduced for 2h in H_2/Ar = 2:1 in the low pressure setup at temperatures ranging from 240 to 400°C. Higher temperatures are less relevant for FTO and could be more complicated due to the titania phase change from anatase to rutile above 465°C. [44] After the reduction the catalysts were exposed to air and analyzed with TEM and STEM-EDX. Figure 4.10a-c show TEM images of Fe-NP/P25 reduced for 2h at 240, 275 and 300°C. The Fe-NP can still be observed in bright-field TEM after reduction at these temperatures. The obtained particle size distributions as shown in Figure 4.10 g indicates that reduction in H_2 in the temperature range of 240-300°C did not affect the particle size to a large extent. Moreover, no large particles were found for these temperatures using STEM-EDX maps (Figure 4.10 d-f).

After reducing at 325°C iron oxide particles can still be recognized however, some of the particles seem to have been altered, appearing more flatter or containing more facets. Moreover, in some cases an amorphous phase was found on the edge of titania particles. STEM-EDX maps of the catalyst

reduced at 325°C show that most particles still have a similar size as the fresh catalysts, although some slightly larger (10-20 nm) particles were found occasionally. The particle size distribution determined from both TEM and STEM-EDX is shown in Figure 4.10 n where the average particle size of 8.29 nm is still close to the that of the fresh catalyst. However, the Gaussian fit has a tail towards slightly larger sizes, indicating that particle growth has already been initiated at 325°C. Additionally, in some cases the EDX maps expose iron species present which do not resemble the 8 nm particles at all. Figure 4.10 h shows an EDX map revealing the presence of iron species along the surface of a titania particle, where no defined particles can be found at that location with TEM. This could be an indication of a strong metal-support interaction.

Figure 4.10 i. shows a TEM image of Fe-NP/P25 reduced at 350 °C. Analogous to what is found for the Fe-NP/P90, no Fe particles can be distinguished from the support material. The EDX map bring the larger iron particles to light that have grown during the reduction in H_2 at 350°C. The particle size distribution shows that the particles have grown to 34.3 ± 12.2. This result is in fair agreement with the particle size obtained from the high pressure reduction of Fe-NP/P90 (Figure 4.9). For the Fe-NP/P25 reduced at 400°C similar results were found, but the final particle size is slightly larger with an average of 41.8 ± 10.7 nm. Altough the particles grow during these 2h reduction, the final size is smaller than that of used catalyst where iron particles have grown to up to 100 nm. This difference can simply be explained by the duration that the catalysts were exposed to the reducing environment. Reducing an Fe-NP/P25 catalyst for 16h already causes particles to grow up to 100 nm as shown in Figure 4.11. Simply heating the titania supported Fe-NP to 350°C under inert atmosphere (15 ml/min Ar) does not result in particle growth, see Figure S5 in the supplementary information. This suggests that heat alone is not cause of particle growth for Fe-NP/TiO_2. Moreover, the temperature at which the growth of Fe-NP particles takes place, coincides with the first peak observed in a temperature programmed reduction experiment of Fe-NP/TiO_2 as shown in Figure S7 of the supplementary information.

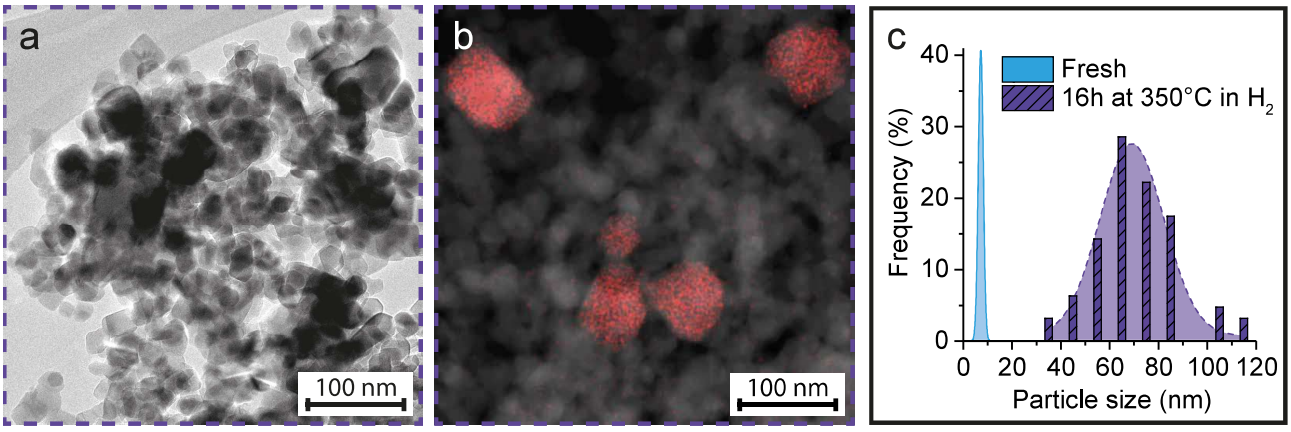

Figure 4.11: a) TEM image and **b)** STEM-EDX map of P25 supprted Fe-NP reduced for 16h 350°C.**c)** The obtained particle size distribution shows that the longer reduction time results in the growth of Fe particles to up to 100 nm, similar to what is observed for the used catalyst.

Fe-NP/Ox50-2 was also subjected to a 2h reduction in H_2 at various temperatures (240, 350 and 550°C). Figure 4.12 shows TEM images of the reduced silica supported catalyst. After reduction at 240°C the particles are still spherical and have a particle size of 7.4 nm which is comparable with the the unreduced catalyst with an average particle size of (7.2 nm). Likewise, no particle growth was expected for the reduction at 350°C, as this was not observed for the used catalyst, see Figure 4.8d-f. The acquired particle size distribution illustrates that Ox50 supported Fe-NP reduced at 350°C indeed retained their size for the most part. Only a few slightly larger particles of 10-14 nm were found. A temperature programmed reduction experiment of Fe-NP/Ox50 showed a maximum at a slightly higher temperatures (≈ 385°C) compared to that of Fe-NP/P25 (≈ 340°C), see Figure S7 in the supplementary information. Therefore, the stability of Ox50 further investigated with a higher reduction temperature. After a reduction in H_2 for 2h at 550°C particle growth was observed, albeit

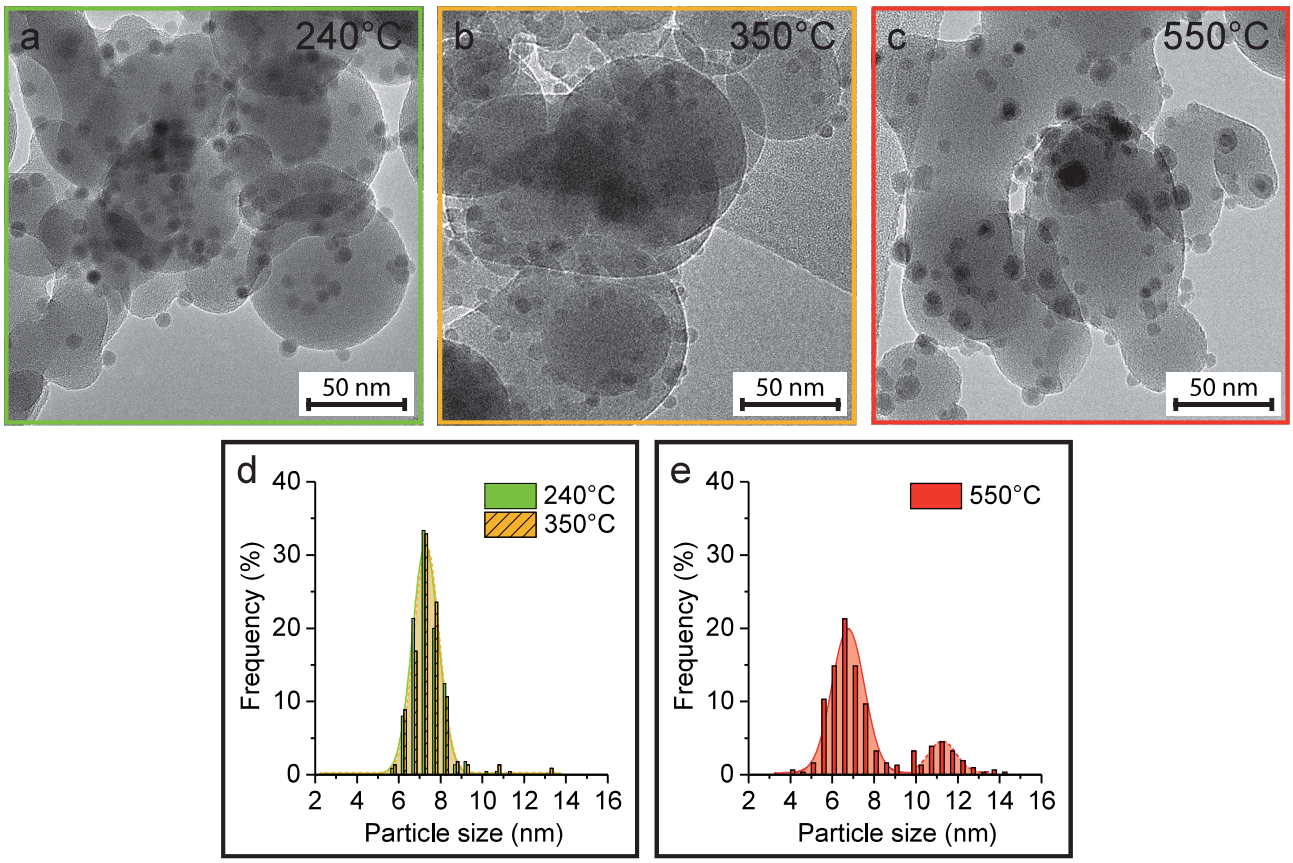

Figure 4.12: TEM images of Fe-NP/Ox50-2 reduced for 2h at **a)** 240°C, **b)** 350°C and **c)** 550°C. **e & f)** Particle size distributions obtained from the TEM images. While particle growth is observed for Fe-NP/TiO_2, SiO_2 supported Fe-NP remain stable after reduction in H_2 at 350°C. Even after a reduction at 550°C, only a part of the iron particles have grown slightly resulting in a bimodal particle size distribution.

to a much lesser extent then is observed for the titania supported Fe-NP. TEM images images show iron(oxide) particles with sizes between 4 and 9 nm as well as core-shell particles of 10-14 nm resulting in a bimodal distribution as displayed in Figure 4.12e.

4.3.3 Reduction with higher weight loading

So far all samples had a similar Fe loading per surface area. A P25 supported catalyst with a higher loading of ≈ 9wt.% iron was also prepared to investigate the effect of the loading on particle growth. The higher loading was obtained by supplying less support material during the attachment step while keeping the other parameters constant. Despite the higher weight loading the size of the iron oxide particles did not change significantly during the attachment, see Figure S1f in the supplementary information. The Fe-NP/P25 with higher Fe loading was reduced in H_2 at 350°C for 2h. The reduced catalyst contains Fe-NP that remained unaffected for the most part as observed by TEM (Figure 4.13a). However, STEM-EDX maps also reveals the presence of larger iron particle, see Figure 4.13b. Measuring the diameter of the small particles from both the TEM images (n=175) and the larger particles from the STEM-EDX maps (n=61) results in a bimodal size distribution as shown in Figure 4.13c. The particles with sizes smaller than 20 nm have an average particle size of 6.6 ± 1.5 nm while the particles of the pristine sample had an average size of 7.5 ± 1 nm. On the other hand the growth of the larger particles have an average particle size of 31.8 ± 8.0 nm. This is similar to the growth observed in the previous experiments with 3wt.% iron (Figure 4.3.2), where an average particle size of 34.3 ± 12.2 nm was found after the reduction in H at 350°C.

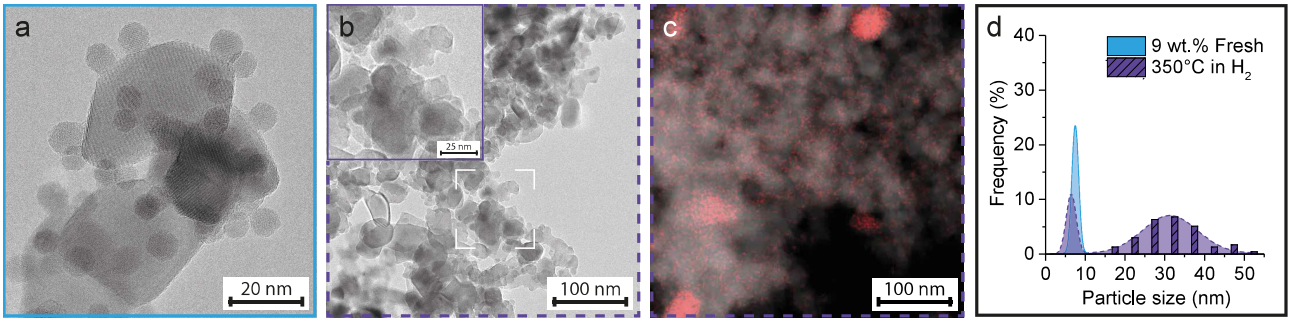

Figure 4.13: a) TEM image of the fresh Fe-NP/P25-HL with an approximate Fe loading of 9wt.%. **b)** TEM image of the Fe-NP/P25-HL reduced in H2 at 350°C. The inset shows a magnification of the area indicated by the white corner which contains Fe-NP that appear unchanged after the reduction. **c)** STEM-EDX map of the reduced catalyst revealing larger iron particles. **d)** Particle size distribution of the reduced catalyst compared to the fresh catalyst..

4.3.4 Reduction in CO

Particle growth of Fe-NP/TiO_2 already occurs during the reduction step. The remaining questions are what is causing the growth and why is it not observed to such extent for Fe-NP/SiO_2. One factor that commonly influence particle growth is the presence of water. Nazila et. al. showed that the presence of water accelerates the growth of titania supported gold particles. [8] The Fe-NP/P25 were not dried before employing them in the FTO reaction or before subjecting them to the reduction treatments and could have contained water. Moreover, H_2O is formed when reducing oxides with H_2. Additionally, water is also produced during the FTO reaction (Equation 4.1).

$$nCO + 2nH_2 \rightarrow C_nH_{2n} + nH_2O \tag{4.1}$$

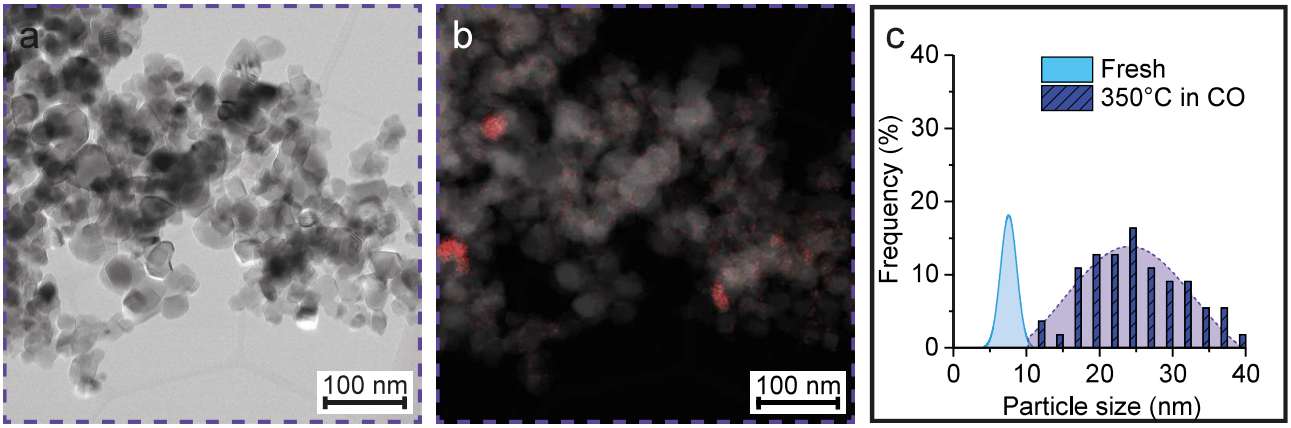

Figure 4.14: a) TEM image and **b)** STEM-EDX map of titania supported Fe-NP (Fe-NP/P25-1) reduced for 2h at 350°C in CO:Ar = 2:1. **c)** Particle size distribution of the fresh and reduced catalyst, showing growth of the iron particles in the absence of water.

In this experiment the goal was to eliminate the presence of water entirely. Fe-NP/P25 were first dried in the low pressure setup for 2h at 350°C. This heat treatment does not affect the particles as confirmed by a blank experiment, Figure S5 in the supplementary information. To prevent water from being produced during the reduction, CO was chosen as reducing agent. Analysis with TEM and STEM-EDX show that particle growth occurs even without the presence of water. A broad size distribution with particles of up to 40 nm were obtained. This is slighlty smaller than the largest particles (60 nm) observed after the reduction in H_2. While water could still have a minor influence on the particle growth, the results of this experiment strongly suggest that not the production of water, but the reduction of iron oxide itself is key to understanding particle growth on titania supports.

4.4 Explaining particle growth of Fe-NP/TiO_2

4.4.1 Semi-quantitative EDX

STEM-EDX maps showed iron signals at location where no actual particles were observed, particularly at reduction temperatures above 325°C. Figure 4.15 a and b show an example of an area scanned (red outlined square) not containing visible particles and the corresponding spectrum of this area. The spectrum confirms the presence of Ti with a peak ≈ 4.5 keV and a small amount of Fe with a peak at 6.4 keV. These results were quantified by taking the average iron counts in the subareas that don't contain iron particles, converting them to a weight percentage relative to TiO_2 and dividing this by the total iron content (also in wt.%) of the scanned area. This yields a percentage of iron that has migrated to the support material.

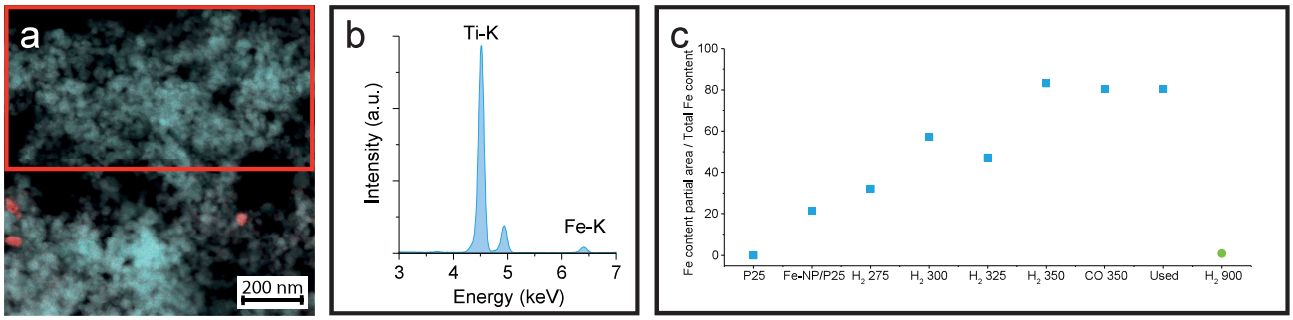

Figure 4.15: **a)** Example of a subarea that does not contain iron particles. **b)** EDX spectrum corresponding to the subarea of **a)**. **c)** The quantified migration of Fe to the support material expressed as the wt.% of Fe in subareas containing no particles divided by the wt.% of Fe in the total scanned area.

Figure 4.15c shows the results of this quantification method for bare support, Fe-NP/P25 reduced in H_2 at 275, 300, 325, 350, in CO at 350°C, Fe-NP/P25 used and Fe-NP/Ox50 reduced during a TPR experiment up to 900°C. For the bare support no iron should be present in the sample and the calculated weight percentage of 0.04 is set as the background signal. A fresh Fe-NP/P25 catalyst already contains roughly 20% iron. After reduction at 275°C the Fe content is still relatively low with ≈ 30%. For reduction treatments at higher temperatures the Fe content in areas that do not contain Fe particles increases drastically to up to 80% for reductions at 350°C in H_2 and CO as well as the used catalyst from the low pressure setup.

In contrast, the migration of Fe to the support for Fe-NP/Ox50 remains below 1% even for a sample reduced in H_2 while heating to 900°C with a heating ramp of 5°C/min. This method of quantifying the amount of iron not present as particles is of course error prone, especially at higher reduction temperatures, due to the fact that there might still be some particles in the scanned areas that were difficult to observe in the bright field TEM images. Additionally for the lower temperatures, particles are distributed across most of the titania support, causing the scanned areas to possibly also contain some particles. Although this method is only semi-quantitative, the observed trends are still an indication that iron is present as atomically small species dispersed over the TiO_2 support.

Table 4.4. Mössbauer parameters

Sample	IS (mm·s-1)	QS (mm·s-1)	Hyperfine field (T)	(mm·s-1)	Phase	Spectral contribution (%)
Fe-NP/Ox50						
	0.34	0.04	49.8	0.88	Fe3+	54
240°C	0.83	-0.11	45.6	0.88	Fe2+	22
	1.16	0.06	31.1	0.88	Fe2+	24
	0.01	-	34.4	0.44	Fe0	21
300°C	1.06	2.35	-	1.04	Fe2+	15
	1.22	-0.28	35.8	0.87	Fe2+	30
	1.2	0.07	31.3	0.87	Fe2+	34
	0.01	-	34.5	0.44	Fe0	41
350°C	1.07	2.39	-	1.04	Fe2+	12
	1.2	-0.24	35.7	0.9	Fe2+	26
	1.22	0.15	31	0.9	Fe2+	21
Fe-NP/P25						
240°C	1.24	2.95	-	0.58	Fe2+	41
	0.44	-0.1	48.5	1.18	Fe3+	59
300°C	1.14	2.65	-	0.58	Fe2+	74
	0.48	-0.32	50	0.93	Fe3+	26
350°C	0.01	-	34.5	0.31	Fe0	32
	1	2.14	-	0.87	Fe2+	68

4.4.2 Mössbauer spectroscopy

Another way to investigate the reduction behaviour of titania and silica supported Fe-NP is with Mössbauer spectroscopy. In this study the iron species in the catalyst were probed after reduction in H_2 at 240, 300 and 350°C. The obtained Mössbauer spectra are shown in Figure 4.16 and the Mossbauer parameters obtained from the spectra are listed in Table 4.4. For the silica supported catalyst reduced at 240°C three sextuplets were obtained. The sextuplet with a hyperfine field of 45.6 is characteristic for an Fe^{2+} component of magnetite (purple subspectrum). The Fe^{3+} sextuplet (hyperfine field = 49.8 T) likely contains contributions from both magnetite and maghemite (pink subspectrum). A third sextuplet with a hyperfine splitting of 31 T was fitted and is attributed to Fe^{2+} present as FeO, wüstite (blue subspectrum).

After the second reduction step at 300°C the spectral contribution of magnetite and maghemite species have diminished, while the spectral contribution of wüstite sextuplet has increased from 24 to 34%. Additionally, two other wüstite signals were observed; a second sextuplet with a hyperfine splitting of 35 T, as well as a doublet with a quadrupole splitting (QS) of 2.35 mm/s. Moreover, a sextuplet with a hyperfine splitting of 34.4 T and an isomer shift 0.01 characteristic for Fe^0 has appeared. So after reduction at 300°C, magnetite and maghemite were already reduced to wüstite and metallic iron. Subsequently reducing Fe-NP/Ox50 at 350°C yields a similar spectrum, albeit with higher degree of reduction as concluded from the increase of the spectral contribution of Fe^0 to 32%.

For Fe-NP/P25 the Mössbauer spectra contain a smaller variety of signals, see Figure 4.16b. After the reduction in H_2 at 240°C a sextuplet related to Fe^{3+} is observed, which could be present in both the magnetite or hematite phases. Additionally, a doublet with a quadrupole splitting of 2.95 mm/s was observed. This value is quite different from the wüstite doublet with a QS of 2.35 and 2.39 observed for the Fe-NP/Ox50 reduced at 300°C and 350°C respectively.

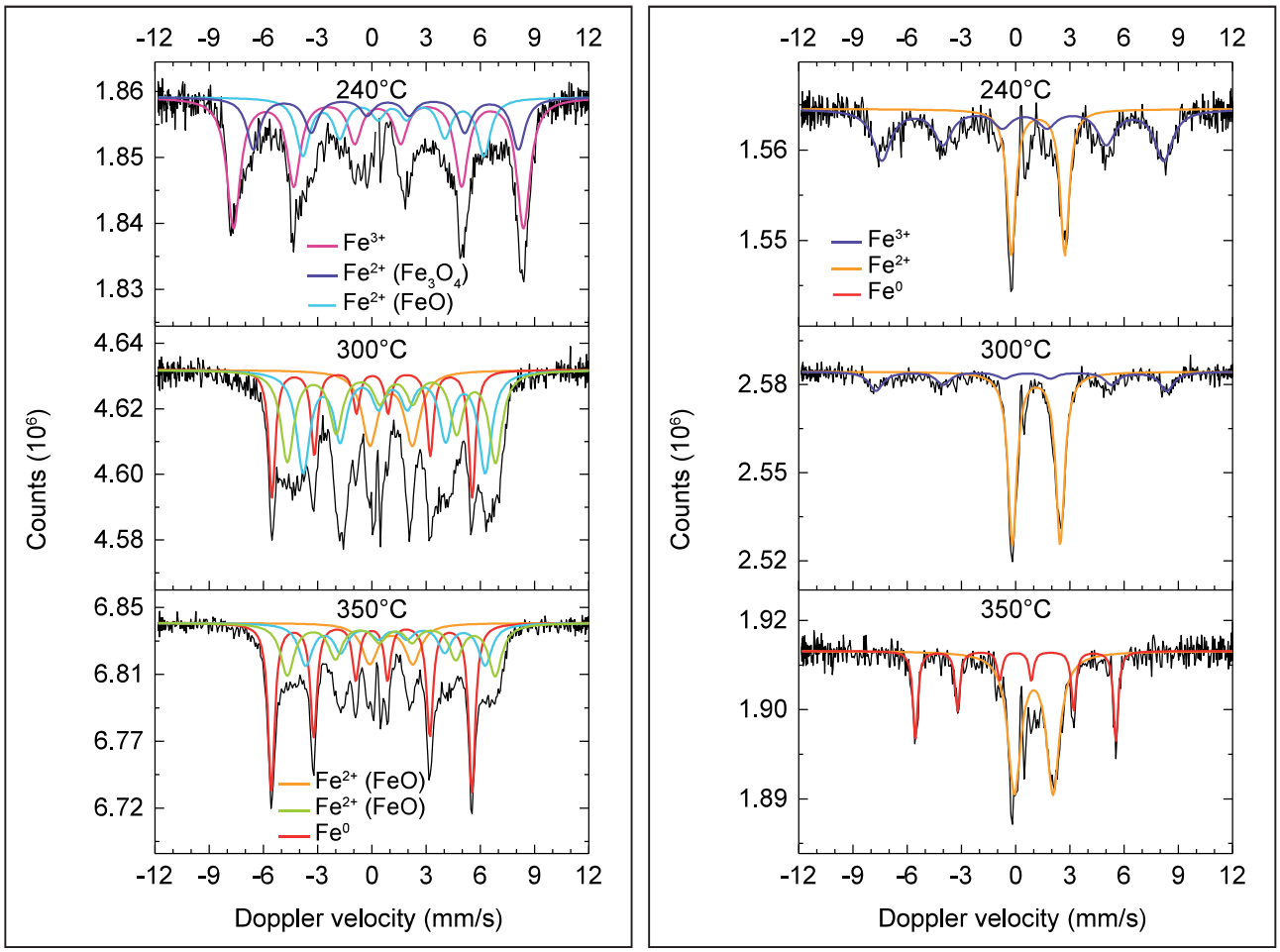

Figure 4.16: Mössbauer spectra of **a)** Fe-NP/Ox50-Mössbauer and **b)** Fe-NP/P25-Mössbauer sequentlially reduced in H_2/Ar= 2 at 240, 300 and 350°C. After each 2h reduction step the sample was cooled down to 120 K before acquiring a spectrum and ramping to the next temperature.

Reducing the Fe-NP/P25 at 300°C results in a lower spectral contribution of the Fe^{3+} species and a higher contribution of the doublet, now with a QS of 2.65 mm/s. After this reduction step, no sextuplet characteristic for metallic iron is present, in contrast to the silica supported Fe-NP.
After the final reduction step at 350°C a characteristic Fe^0 sextuplet with a hyperfine field of 34.5 is observed similar to that in the reduced Fe-NP/Ox50. The doublet remains with a slightly lower spectral contribution of 68% (orange subspectrum), interestingly, the quadrupole splitting has decreased again to 2.14 mm/s.

The Fe^{2+} doublet and its decreasing QS might be key to understanding the difference between the growth observed for Fe-NP/TiO_2 and Fe-NP/SiO_2. The results so far show that a reducing atmosphere at temperatures above 325°C lead to particle growth for Fe-NP/TiO_2. This observation suggest that an interaction between the titania support and reduced iron species is causing or accelerating the growth of the nanoparticles. Possible interactions between iron and titania include: 1) The formation of a Fe_3TiO_6 solid solution with an inverse spinel structure by substitution of Fe^{3+} in octahedral sites of Fe_3O_4 for Ti^{4+}, see Equation 4.2. [45] and 2) the incorporation of Fe^{3+} into the TiO_2 matrix to charge-compensate oxygen vacancies created at higher temperatures in oxygen poor atmospheres. [46, 47]

$$TiO_2 + (Fe^{3+})_T(Fe^{2+}, Fe^{3+})_O O_4 \rightarrow (Fe_3{}^+)_T(Fe^{2+}, Ti^{2+})_O O_6 \tag{4.2}$$

In both processes Fe^{3+} plays an important role, which should result in a signal in the Mössbauer spectrum. For the Fe_3TiO_6 a sextuplet with a slightly higher quadrupole splitting than bulk Fe_3O_4 is expected [45], while a high spin (S=5/2) Fe^{3+} as dopant in TiO_2 would give rise to a doublet with an isomer shift of approximately 0.4 mm/s and a QS of 0.6 mm/s. [48] After reducing Fe-NP/TiO_2 in H_2 at 350°C both of these Fe^{3+} signals are absent, eliminating these interactions as a cause of particle growth.

$$Fe_2O_3 + 2\ TiO_2 + H_2 \rightarrow 2\ FeTiO_3 + H_2O \tag{4.3}$$

Another possible interaction 3) is the reduction of Fe^{3+} to Fe^{2+} and subsequent reaction with TiO_2 to form an $FeTiO_3$ phase, see Equation 4.3. In literature a doublet with an IS of around 1.0-1.3 mm/s and a QS of approximately 0.6-0.7 mm/s has been assigned to Fe^{2+} in this $FeTiO_3$ phase. [45, 49, 50]. However, these measurements were taken at room temperature. Lower measurement temperatures can shift the QS to higher values, for instance at 50 K an QS of 1.4 mm/s can be found. The Mössbauer spectra in present study were taken at 120 K, therefor the QS of crystalline $FeTiO_3$ will not exceed a value of 1.4 mm/s. Thus, the doublets observed for the reduced Fe-NP/P25 with a QS ranging from 2.95 to 2.14 for higher reduction temperatures can not be assigned to crystalline $FeTiO_3$. However, the decreasing QS could indicates an increasing crystallinity for higher reduction temperatures. So while no crystalline $FeTiO_3$ can be observed, the presence of amorphous $FeTiO_3$ cannot be excluded. Additionally, thermodynamic calculation also show than an FeO*TiO_2 phase is stable in an excess of H_2 at elevated temperatures, see supplementary information S9. Moreover, M. Rayner et. al. detected an amorphous phase with in-situ XRD for titania supported iron catalyst arising at 360°C during a reduction in H_2. [9]. Another viable interpretation of the doublet is Fe^{2+} in surface sites of the TiO_2 support. X. Gao et. al. reported an IS of between 0.9 and 1.10 mm/s and a QS ranging from 1.5 to 1.8 mm/s (recorded at room temperature) for such surface species after reduction in H_2.

4.4.3 Proposed mechanism for growth

Extreme particle growth of Fe-NP/TiO_2 was observed during the reduction at temperatures above 325°C. Fe-NP/SiO_2 on the other hand remained stable and only grow slightly even at reduction temperatures of 550°C, see Figure 4.12. This indicated that the reduction plays a vital role in the particle growth of Fe-NP/TiO_2. Semi-quantitative EDX analysis of reduced samples indicated the presence of iron species dispersed on the TiO_2 supports, but almost none for SiO_2. Combining these observations with the Mössbauer spectroscopy results described in the previous section leads to the following proposed growth mechanism, see Figure 4.17.
In a reducing atmosphere (H_2 or CO) at elevated temperature the Fe-NP reacts with the TiO_2 to form an amorphous $FeTiO_3$ on the surface of support. From this amorphous phase mobile Fe^{2+} are more easily isolated than from iron oxide nanoparticles. Fe^{2+} can then hop from TiO_2 surface site to surface site until they reach and attach to an iron particle that is still present or has already grown, in a way similar to the Ostwald ripening mechanism. This surface species assisted Ostwald ripening ultimately leads to the formation of extremely large particles as observed in this study.

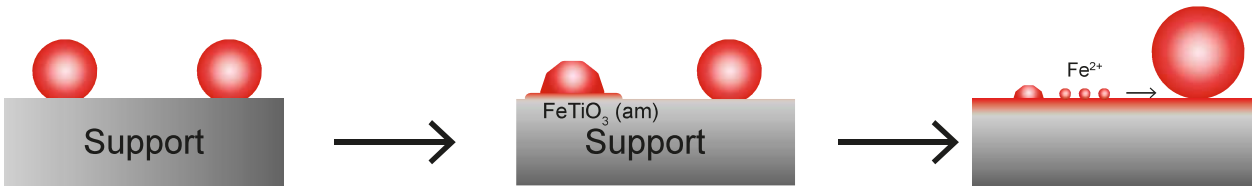

Figure 4.17: Proposed mechanism for the particle growth observed of Fe-NP/TiO_2 in reducing atmospheres at elevated temperatures.

5. Conclusions

SiO_2 and TiO_2 supported iron oxide nanoparticles (Fe-NP) were prepared and used as model system to study particle growth during activation and the FTO reaction. Colloidal Fe-NP of approximately 7 nm were successfully synthesized form iron pentacarbonyl using the heating-up method. Comparable SiO_2 and TiO_2 support materials for the model system were chosen based on BET surface area and pore volume obtained with nitrogen physisorption and the particle size distribution obtained from transmission electron microscopy (TEM) images. Attachment of the prepared Fe-NP to Aerosil Ox50, Aerosil 90, Aerosil 130, P25 and P90 did not change to size of the iron oxide particles. Moreover, a similar Fe loading per surface area was obtained for all catalysts, despite the difference in Hamaker constant between SiO_2 and TiO_2. The catalytic performance of the model catalysts was evaluated in the FTO reaction. In general the activity of the colloidal catalyst after 100h were comparable with each other as well as with reference catalysts obtained via impregnation with an $Fe(NO_3)_3$ solution of either Ox50 and P25. Only the activity of Fe-NP/P25 was significantly lower than that of Fe-NP/Ox50. However, the titania supported catalysts; Fe-NP/P25 and Fe-NP/P90 exhibited a lower methane selectivity and a higher selectivity towards C5+ than SiO_2 supported catalysts.

Although SiO_2 and TiO_2 supported Fe-NP appeared quite similar in terms of Fe-NP size, Fe loading per surface area and to some extent the activity and selectivity in the FTO reaction, a remarkable distinction was found when comparing the used catalysts. Fe-NP/SiO_2 retained their size of approximately 7 nm after 100h under reaction conditions as determined with TEM. On the other hand STEM-EDX maps revealed that Fe-NP on both P25 and P90 had grown tremendously, with particle sizes up to 100 nm. Further experiments showed that the particle growth of Fe-NP/TiO_2 already occurs during a 2h reduction step in H_2 at temperatures above 325°C. The average particle sizes of 2h reduction steps are smaller than those observed in the used catalyst, however longer reduction times will lead to more growth. For instance, particles of up to 100 nm, similar to that of the spent catalysts, were observed for a 16 h reduction in H_2 at 350°C. In contrast, only minor growth (up to 14 nm) was observed for Fe-NP/SiO_2 even after a 2h reduction in H_2 at 550°C.

The presence of water was ruled out as the cause of particle growth Fe-NP/TiO_2, because larger particles were also observed for Fe-NP/TiO_2 pre-dried and reduced in a flow of CO at 350°C. A semi-quantitative STEM-EDX analysis of reduced Fe-NP/TiO_2 revealed an increasing amount of iron species present at locations where no particles are found in TEM mode with increasing reduction temperatures. Mössbauer spectroscopy was employed to determine the nature of the iron species present in Fe-NP/TiO_2 and Fe-NP/SiO_2 reduced at 240, 300 and 350°C. For silica supported Fe-NP, metallic iron and Fe^{2+} in the wüstite (FeO) phase present after a reduction in H_2 at 300°C and 350°C. For Fe-NP/TiO_2, metallic iron is only present after reduction at 350°C. More interestingly, a doublet signal with a decreasing quadrupole splitting (2.95, 2.65 2.14 mm/s) upon increasing reduction temperature was present for Fe-NP/TiO_2. This signal has been assigned to Fe^{2+} present as amorphous $FeTiO_3$ or as surface species. These finding were key in elucidating the particle growth observed for Fe-NP/TiO_2 and why it did not occur for Fe-NP/SiO_2.

6. Outlook

More experiments could be done to confirm if the growth is indeed caused by the formation of amorphous $FeTiO_3$ and Fe^{2+} surface species. For instance, XPS can be used to probe the surface species as the escape depth of the photo-electrons is only a couple of nm. Another possibility and complementary to the semi quantitative EDX experiment would be electron energy loss spectroscopy combined with STEM. While both EDX and EELS allow for local characterization of the elements in a sample, EELS could yield more information on the chemical bonding and valency of the iron present on or in the TiO_2 support. An in-situ bulk analysis technique such as in-situ XRD could also give some insight on crystal phase during the reduction, as shown by M.K. Rayner et al. [9] Alternatively, more reduction experiment could be carried out at temperatures in the range between 325°C and 350°C, where the most of particle growth took place for Fe-NP/TiO_2. Also, the identical location TEM method as described in S8 of the supplementary information, could be improved, however our results with IL-TEM were not representative for the regular reduction experiments in the high and low pressure setups. Finally, the implementation of colloidal particles as a model system has proven worthwhile and can be applied to explore particle growth of many other supported catalyst and increase our understanding of these interesting systems.

Acknowledgements

I would like to thank Dennie Wezendonk for performing the TGA-MS experiments, Coen Mulder for the ICP data and dr. Iulian Dugulan from Delf University for conducting and analysis of the Mössbauer spectroscopy experiments. Appreciation for Tom van Deelen, Carlos Hernández Mejía and Lennart Weber for their help with the catalytic setup and additional thanks to dr. Jovana Zečević and Savannah Turner for useful discussion and dr. Baira Donoeva for her role as second supervisor. Finally I would like to thank the Inorganic Chemistry and Catalysis group at Utrecht University for having me during this project.

Bibliography

[1] H. M. T. Galvis and K. P. de Jong, "Catalysts for Production of Lower Olefins from Synthesis Gas : A Review," *ACS Catalysis*, vol. 3, pp. 2130–2149, 2013.

[2] M. Bender, "An Overview of Industrial Processes for the Production of Olefins – C 4 Hydrocarbons," no. 4, pp. 136–147, 2014.

[3] G. A. Olah, A. Goeppert, and G. K. S. Prakash, "Chemical Recycling of Carbon Dioxide to Methanol and Dimethyl Ether : From Greenhouse Gas to Renewable , Environmentally Carbon Neutral Fuels and Synthetic Hydrocarbons Chemical Recycling of Carbon Dioxide to Methanol and Dimethyl Ether : From Greenhouse," *Journal of Organic Chemistry*, vol. 74, no. 2, 2009, pp. 487–498, 2009.

[4] Y. Zhang, Q. Sun, J. Deng, D. Wu, and S. Chen, "A high activity Cu/ZnO/A1203 catalyst for methanol synthesis: Preparation and catalytic properties," *Applied Catalysis A: General*, vol. 158, pp. 105–120, 1997.

[5] H. M. Torres Galvis, A. C. J. Koeken, J. H. Bitter, T. Davidian, M. Ruitenbeek, A. I. Dugulan, and K. P. De Jong, "Effect of precursor on the catalytic performance of supported iron catalysts for the Fischer-Tropsch synthesis of lower olefins," *Catalysis Today*, vol. 215, pp. 95–102, 2013.

[6] R. Ouyang, J. X. Liu, and W. X. Li, "Atomistic theory of ostwald ripening and disintegration of supported metal particles under reaction conditions," *Journal of the American Chemical Society*, vol. 135, no. 5, pp. 1760–1771, 2013.

[7] K. P. D. Jong, T. W. V. Deelen, J. J. Nijhuis, N. A. Krans, and J. Zec, "Preparation of Cobalt Nanocrystals Supported on Metal Oxides To Study Particle Growth in Fischer - Tropsch Catalysts X," vol. 10589, 2018.

[8] N. Masoud, T. Partsch, K. P. D. Jong, and P. E. D. Jongh, "Thermal stability of oxide-supported gold nanoparticles," pp. 105–114, 2019.

[9] M. K. Rayner and G. David, "non-ambient crystallography In-situ X-ray diffraction activation study on an Fe / TiO 2 pre-catalyst non-ambient crystallography," pp. 498–509, 2014.

[10] T. Hyeon, "Chemical synthesis of magnetic nanoparticles," *Chemical Communications*, no. 8, pp. 927–934, 2003.

[11] M. Casavola, J. Hermannsdörfer, N. De Jonge, A. I. Dugulan, and K. P. De Jong, "Fabrication of Fischer-Tropsch Catalysts by Deposition of Iron Nanocrystals on Carbon Nanotubes," *Advanced Functional Materials*, vol. 25, no. 33, pp. 5309–5319, 2015.

[12] S. Mourdikoudis and L. M. Liz-Marzán, "Oleylamine in nanoparticle synthesis," *Chemistry of Materials*, vol. 25, no. 9, pp. 1465–1476, 2013.

[13] W. W. Yu, J. C. Falkner, C. T. Yavuz, and V. L. Colvin, "Synthesis of monodisperse iron oxide nanocrystals by thermal decomposition of iron carboxylate salts," *Chemical Communications*, no. 20, p. 2306, 2004.

[14] C.-J. Jia and F. Schüth, "Colloidal metal nanoparticles as a component of designed catalyst," *Physical Chemistry Chemical Physics*, vol. 13, no. 7, p. 2457, 2011.

[15] J. Polte, "Fundamental growth principles of colloidal metal nanoparticles – a new perspective," pp. 6809–6830, 2015.

[16] V. K. Lamer and R. H. Dinegar, "Theory, Production and Mechanism of Formation of Monodispersed Hydrosols," *Journal of the American Chemical Society*, vol. 72, no. 11, pp. 4847–4854, 1950.

[17] S. G. Kwon, Y. Piao, J. Park, S. Angappane, Y. Jo, N.-m. Hwang, J.-g. Park, and T. Hyeon, "Kinetics of Monodisperse Iron Oxide Nanocrystal Formation by " Heating-Up " Process," no. c, pp. 12571–12584, 2007.

[18] S. G. Kwon and T. Hyeon, "Formation mechanisms of uniform nanocrystals via hot-injection and heat-up methods," *Small*, vol. 7, no. 19, pp. 2685–2702, 2011.

[19] J. Park, K. An, Y. Hwang, J. E. Park, H. J. Noh, J. Y. Kim, J. H. Park, N. M. Hwang, and T. Hyeon, "Ultra-large-scale syntheses of monodisperse nanocrystals," *Nature Materials*, vol. 3, no. 12, pp. 891–895, 2004.

[20] R. Hufschmid, H. Arami, R. M. Ferguson, M. Gonzales, E. Teeman, L. N. Brush, N. D. Browning, and K. M. Krishnan, "Synthesis of phase-pure and monodisperse iron oxide nanoparticles by thermal decomposition," *Nanoscale*, vol. 7, no. 25, pp. 11142–11154, 2015.

[21] H. M. T. Galvis, "Supported Iron Nanoparticles as," *Science*, vol. 835, no. February, pp. 1–5, 2012.

[22] "NSHS-Science standard enthalpy of formation for various compounds standard enthalpy of formation for atomic and molecular ions." `http://nshs-science.net.` Accessed: 12-6-2018.

[23] G. A. Olah, "Beyond Oil and Gas : The Methanol Economy," *Angewandte Chemie*, vol. 44, pp. 2636–2639, 2005.

[24] S. S. Bharadwaj and L. D. Schmidt, "Catalytic Partial Oxidation of Natural Gas to Syngas," *Fuel Processing Technology*, vol. 42, no. 2-3, pp. 109–127, 1995.

[25] M. Hegarty, A. O'Connor, and J. Ross, "Syngas production from natural gas using ZrO2-supported metals," *Catalysis Today*, vol. 42, no. 3, pp. 225–232, 1998.

[26] H. M. Torres Galvis, A. C. Koeken, J. H. Bitter, T. Davidian, M. Ruitenbeek, A. I. Dugulan, and K. P. De Jong, "Effects of sodium and sulfur on catalytic performance of supported iron catalysts for the Fischer-Tropsch synthesis of lower olefins," *Journal of Catalysis*, vol. 303, pp. 22–30, 2013.

[27] T. Herranz, S. Rojas, F. J. Pérez-alonso, M. Ojeda, P. Terreros, and J. L. G. Fierro, "Genesis of iron carbides and their role in the synthesis of hydrocarbons from synthesis gas," vol. 243, pp. 199–211, 2006.

[28] Q. Chang, C. Zhang, C. Liu, Y. Wei, A. V. Cheruvathur, Y. Yun, Y. Yang, and Y. Li, "Relationship between Iron Carbide Phases (ϵ -Fe 2 C , Fe 7 C 3 , and χ - Fe 5 C 2) and Catalytic Performances of Fe / SiO 2 Fischer - Tropsch Catalysts," 2018.

[29] K. Cheng, V. V. Ordomsky, M. Virginie, B. Legras, P. A. Chernavskii, V. O. Kazak, C. Cordier, S. Paul, Y. Wang, and A. Y. Khodakov, "Support effects in high temperature Fischer-Tropsch synthesis on iron catalysts," *Applied Catalysis A: General*, vol. 488, pp. 66–77, 2014.

[30] M. Oschatz, W. S. Lamme, J. Xie, A. I. Dugulan, and K. P. De, "Ordered Mesoporous Materials as Supports for Stable Iron Catalysts in the Fischer – Tropsch Synthesis of Lower Olefins," pp. 2846–2852, 2016.

[31] T. R. Motjope and T. H. Dlamini, "In-situ Mössbauer Spectroscopy of Supported Iron Fischer-Tropsch Catalysts During Activation," vol. 43, 2005.

[32] M. Casavola, J. Xie, J. D. Meeldijk, N. A. Krans, A. Goryachev, J. P. Hofmann, A. I. Dugulan, and K. P. De Jong, "Promoted Iron Nanocrystals Obtained via Ligand Exchange as Active and Selective Catalysts for Synthesis Gas Conversion," *ACS Catalysis*, vol. 7, no. 8, pp. 5121–5128, 2017.

[33] N. A. Krans, E. van der Feltz, J. Xie, A. Dugulan, J. Zečević, and K. de Jong, "Attachment of Iron Oxide Nanoparticles to Carbon Nanotubes and Consequences for Catalysis," *ChemCatChem*, 2018.

[34] L. Bergström, "Hamaker constants of inorganic materials," *Advances in Colloid and Interface Science*, vol. 70, pp. 125–169, 1997.

[35] T. W. Hansen, A. T. Delariva, S. R. Challa, and A. K. Datye, "Sintering of Catalytic Nanoparticles : Particle Migration or Ostwald Ripening ?," vol. 46, no. 8, 2013.

[36] B. Akbari, M. P. Tavandashti, and M. Zandrahimi, "Particle Size Characterization of Nanoparticles – a," *Iranian Journal of Materials Science & Engineering*, vol. 8, no. 2, pp. 48–56, 2011.

[37] B. Inkson, "Scanning electron microscopy (SEM) and transmission electron microscopy (TEM) for materials characterization," *Materials characterization using nondestructive evaluation (NDE) methods*, pp. 17–43, 2016.

[38] "CheEBI chemical entities of biological interest." `https://www.ebi.ac.uk/chebi/searchId.do?chebiId=CHEBI:52623`. Accessed: 18-10-2019.

[39] B. Fultz, "Mössbauer Spectrometry," 2011.

[40] J. R.S. Preston, S.S. Hanna, "Mössbauer Effect in Metallic Iron," *Physical Review*, vol. 128, no. 5, p. 2207, 1962.

[41] R. Buonsanti, V. Grillo, E. Carlino, C. Giannini, M. L. Curri, C. Innocenti, C. Sangregorio, K. Achterhold, F. G. Parak, A. Agostiano, and P. D. Cozzoli, "Seeded growth of asymmetric binary nanocrystals made of a semiconductor TiO2 rodlike section and a magnetic γ-Fe2O 3 spherical domain," *Journal of the American Chemical Society*, vol. 128, no. 51, pp. 16953–16970, 2006.

[42] B. Ohtani, D. Li, and R. Abe, "Journal of Photochemistry and Photobiology A : Chemistry What is Degussa (Evonik) P25 ? Crystalline composition analysis , reconstruction from isolated pure particles and photocatalytic activity test," vol. 216, pp. 179–182, 2010.

[43] A. Ruíz-baltazar, R. Esparza, G. Rosas, and R. Pérez, "Effect of the Surfactant on the Growth and Oxidation of Iron Nanoparticles," vol. 2015, 2015.

[44] S. Bagheri, N. M. Julkapli, S. Bee, and A. Hamid, "Titanium Dioxide as a Catalyst Support in Heterogeneous Catalysis," vol. 2014, 2014.

[45] X. Gao, J. Shen, Y. Hsias, and Y. Chen, "Reduction of Supported Iron Oxide studied by Temperature-programmed Reduction combined with Mossbauer Spectroscopy and X-Ray Diffraction," vol. 9, 1993.

[46] X. Liu, G. Lu, Z. Yan, and J. Beltramini, "Recent advances in catalysts for methanol synthesis via hydrogenation of CO and CO2," *Industrial & engineering ...*, pp. 6518–6530, 2003.

[47] Q. Wu and Q. Zheng, "Creating Oxygen Vacancies as a Novel Strategy To Form Tetrahedrally Coordinated Ti 4+ in Fe/TiO 2 Nanoparticles," no. 1, 2012.

[48] X. H. Wang, J. Li, H. Kamiyama, M. Katada, N. Ohashi, Y. Moriyoshi, and T. Ishigaki, "Pyrogenic Iron (III) -Doped TiO 2 Nanopowders Synthesized in RF Thermal Plasma : Phase Formation , Defect Structure , Band Gap , and Magnetic Properties," no. Iii, pp. 10982–10990, 2005.

[49] L. A. Boot, A. Jos, V. Dillen, and J. W. Geus, "Mössbauer spectroscopic investigations of supported iron oxide dehydrogenation catalysts," vol. 145, pp. 389–405, 1996.

[50] M. Effect, "FeTiO, -eFe, O,," vol. 123, no. 12, pp. 1239–1240, 1961.

[51] S. Yu, T. Zhang, Y. Xie, Q. Wang, X. Gao, R. Zhang, Y. Zhang, and H. Su, "Synthesis and characterization of iron-based catalyst on mesoporous titania for photo-thermal F-T synthesis," *International Journal of Hydrogen Energy*, vol. 40, no. 1, pp. 870–877, 2015.

[52] H.-y. Lin, Y.-w. Chen, and C. Li, "The mechanism of reduction of iron oxide by hydrogen," *Thermochimica*, vol. 400, pp. 61–67, 2003.

7. Supplementary information

S1 Attachment of Fe-NP to support materials

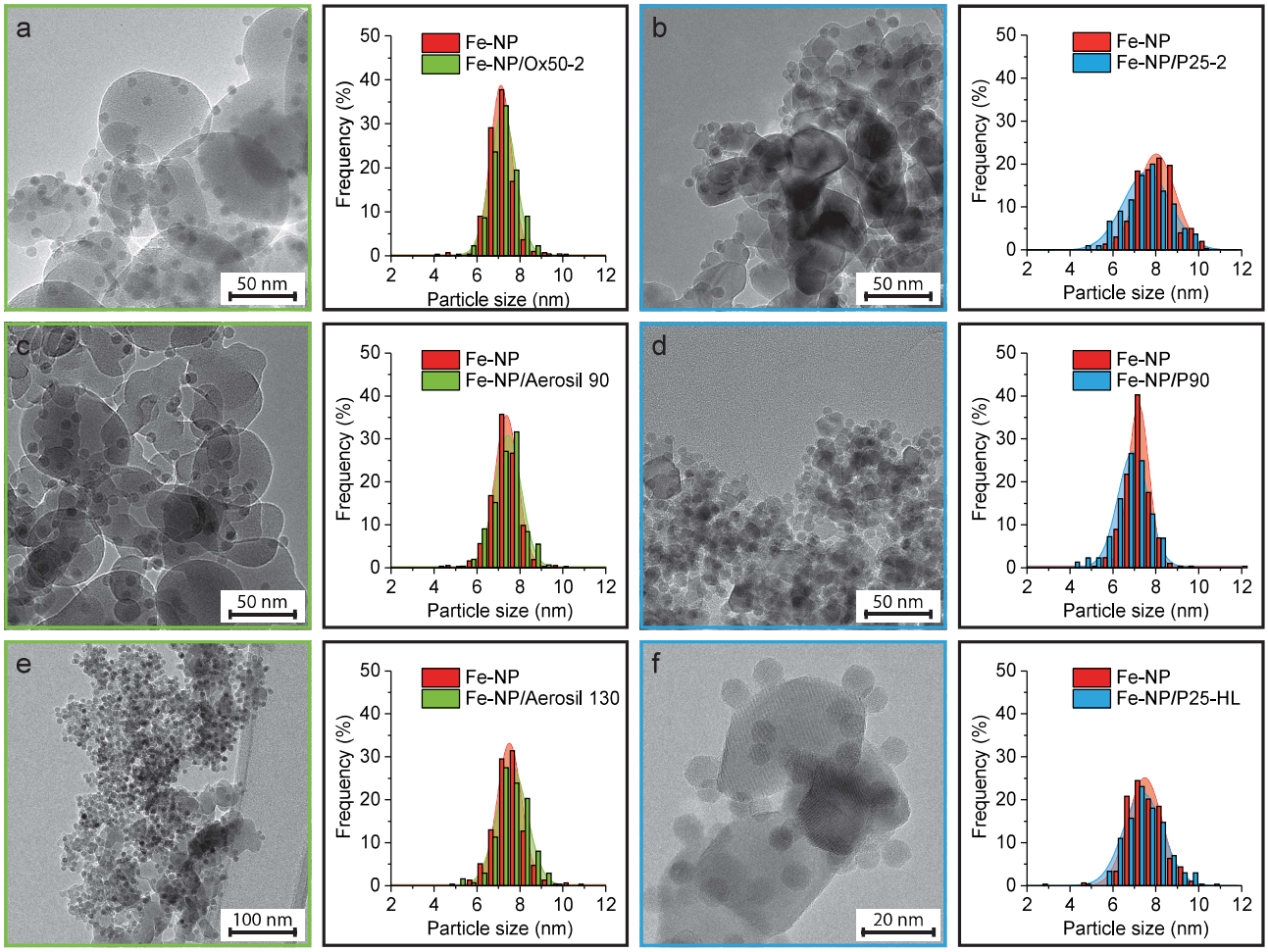

Figure S1: TEM images of Fe-NP attached to support materials and corresponding particle size distributions before and after the attachment. **a)** Fe-NP/Ox50-2, **b)** Fe-NP/P25-2, **c)** Fe-NP/Aerosil 90, **d)** Fe-NP/P90, **e)** Fe-NP/Aerosil 130, **f)** Fe-NP/P25-HL (High loading).

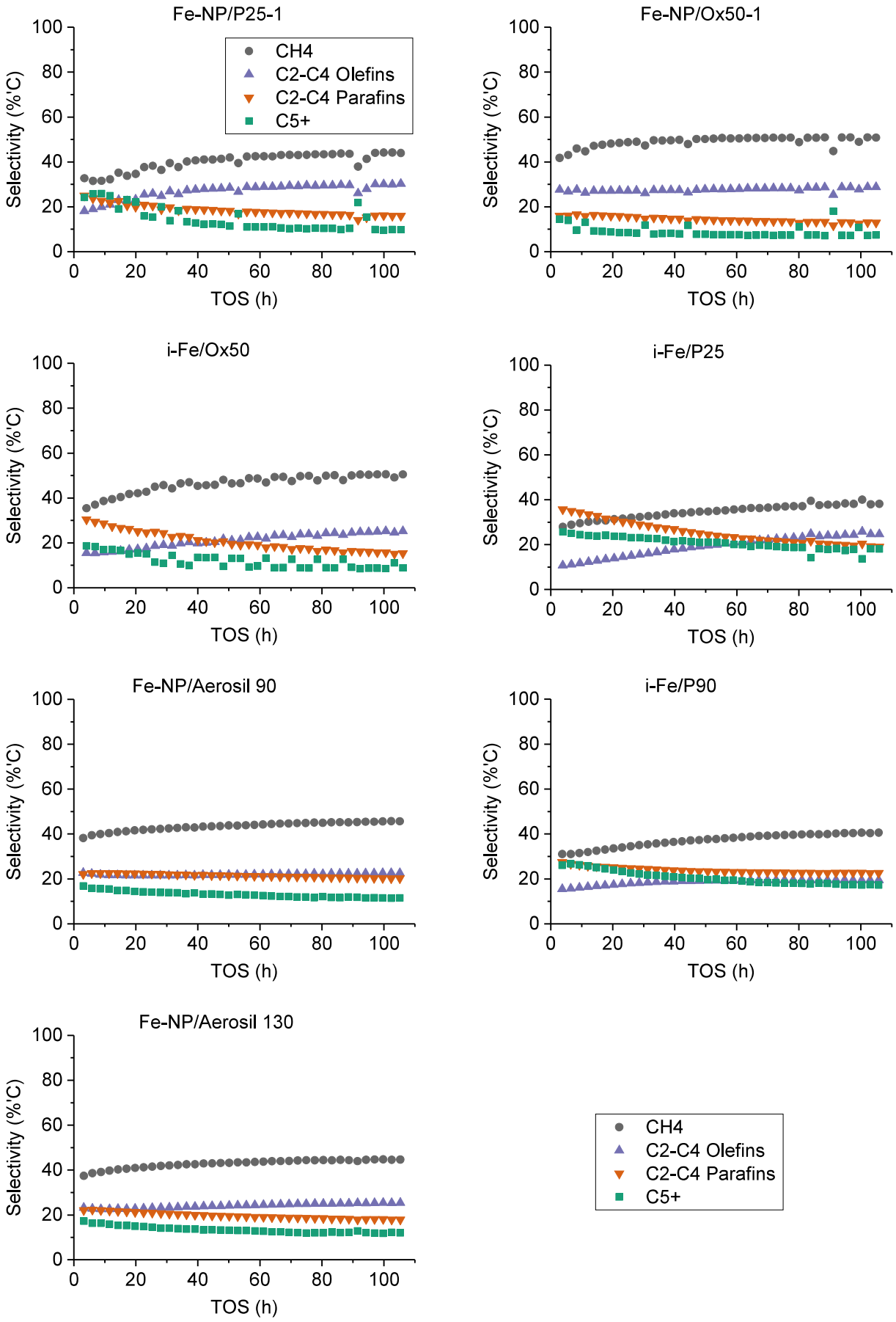

Figure S2: Selectivity of the tested catalysts during the FTO reaction performed under high pressure in the Flowrence Avantium 16-port parallel reactor setup. The figures show the selectivity in terms of % C (excluding the selectivity to CO_2) vs. time on stream (TOS). The type of hydrocarbons is indicated by: **Grey circles)** Methane, **Purple triangles, up)** C2-C4 Olefins, **Orange triangles, down)** C2-C4 Parafins and **Green squares)** C5+.

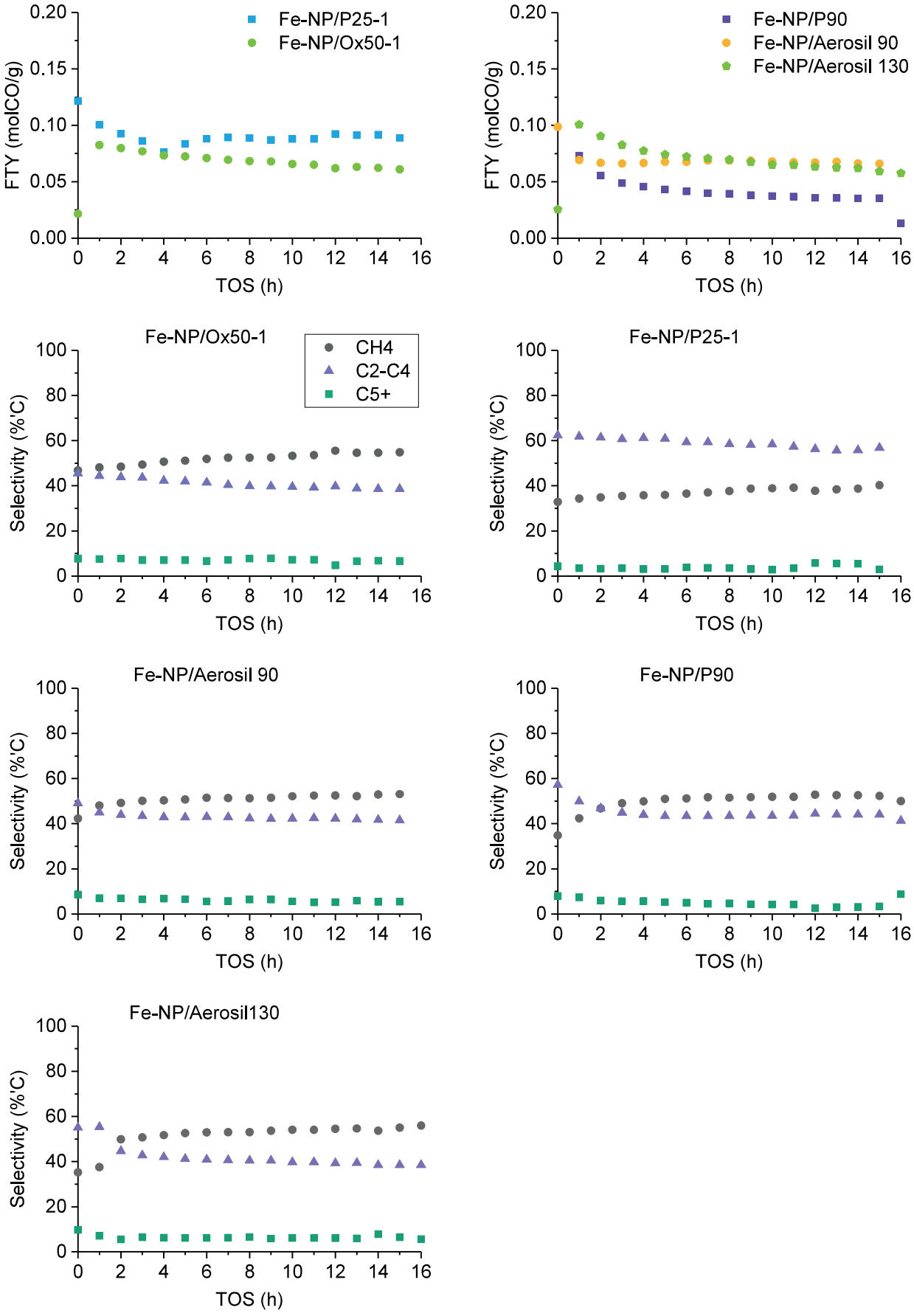

Figure S3: Activity (FTY) and selectivity in %C (excl. CO_2). during the FTO reaction in the low pressure setup. **Grey circles)** Methane, **Purple triangles)** C2-C4 Olefins + Parafins and **Green squares)** C5+.

S4 Low pressure used catalyst

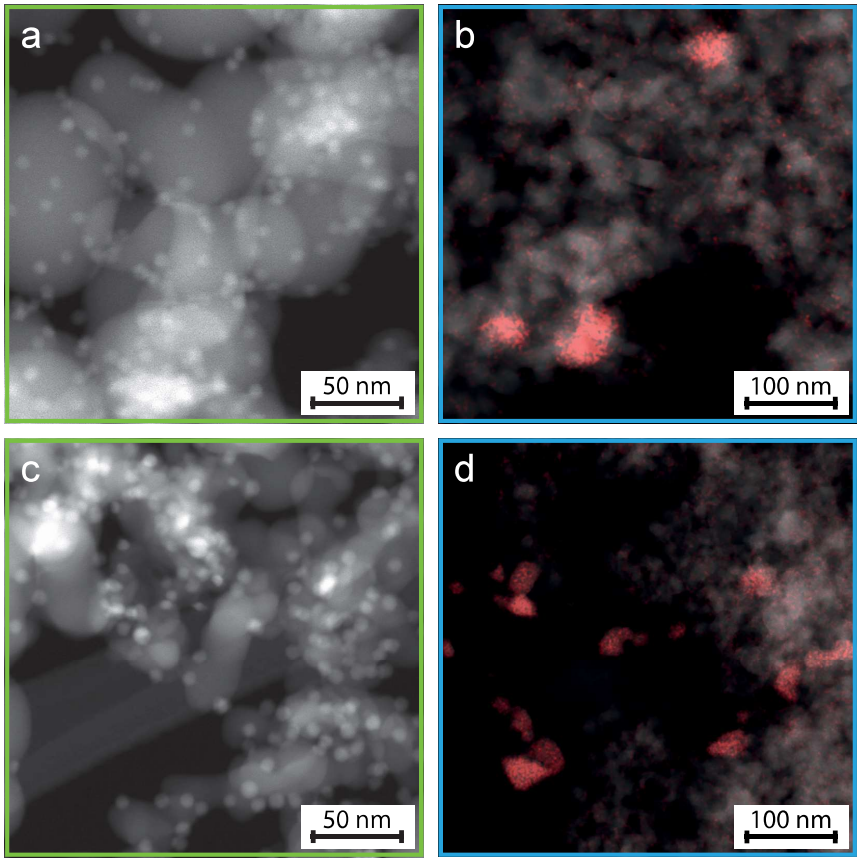

Figure S4: HAAFD-STEM images of **a)** Fe-NP/Ox50, **c)** Fe-NP/Ox90 and EDX maps of **b)** Fe-NP/P25 and **d)** Fe-NP/P90 after 16h of FTO in the low pressure setup.

S5 Heating Fe-NP/P25 in argon

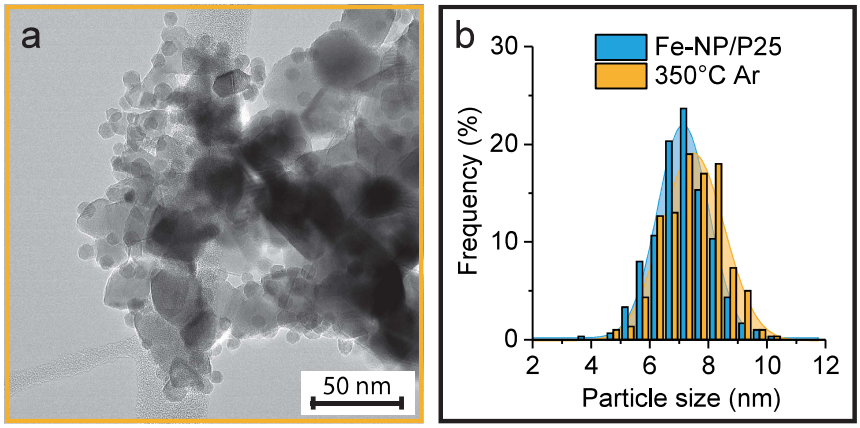

Figure S5: a) TEM image of Fe-NP heated at 350°C for 2h in an argon of 15ml/min and **b)** the obtained particle size distribution before and after heating. No significant particle growth was observed for this blank experiment in inert atmosphere, as opposed to the particle growth observed in reducing atmospheres.

S6 Influence of water

To see if the presence of water enhances particle growth, P25 supported iron oxide particles were reduced in the low pressure setup at 300°C with a water reservoir installed in between the outlet of the mass flow controllers and the inlet of the glass reactor. Figure **??** show a TEM image and STEM-EDX map of the reduced sample. At 300°C small particles can still be seen, similar to the results found with no additional water. The STEM-EDX maps also contain a few slightly larger areas with a signal corresponding to the presence of Fe. It remains unclear if these areas arise from single larger particles or from multiple smaller ones. Water might still play a role, however insignificant compared to the role of H_2 and CO. Silica supported Fe-NP did not grow during the reduction at 350°C. Feeding water vapor in the system did not change this behavior.

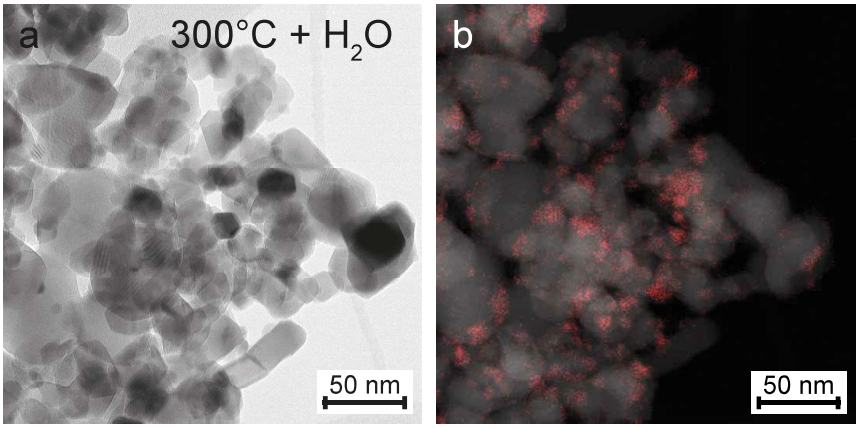

Figure S6: a) TEM image and **EDX map** of Fe-NP/P25 heated at 300°C in H_2 with water introduced into the system.

S7 Temperature programmed reduction

After realizing that the reduction temperature has a great influence on the particle growth for titania, but not for silica supported Fe-NP, the reduction behaviour of iron on these supports was inspected using temperature programmed reduction (TPR). In the order of 25-50 mg of catalyst was reduced in 15 ml/min H_2 while increasing the temperature with 5°C/min. Figure S7 shows the reduction profile for both catalysts. The titania supported catalyst shows a first peak at starting at roughly 300°C and reaching a maximum around 340°C. Which is suspiciously close to the reduction temperature at which extreme particle growth was observed, see Figure 4.10.
The first peak for the silica supported catalyst also starts around 300°C, but the maximum is delayed until 385°C. The area of the peaks was integrated, the ratio between the first peak of the P25 supported catalyst and that of the Ox50 supported catalyst is 1.02. The almost identical peak areas indicating that the amount of iron that is reduced is smilar for both catalysts. At higher temperatures a broad peak is also observed. TPR profiles of iron oxide have been reported in the literature. Generally, the first peak around 300°C is assigned to the reduction of Fe_2O_3 to Fe_3O_4 [51, 52], while the broad peak above 500°C is caused by the subsequent reduction of Fe_3O_4 to metallic iron. A small third peak was also found arising at 400 and 450°C for titania and silica supported Fe-NP respectively. In literature this peak is attributed to the reduction to FeO. While this wustite phase is less stable than magnetite or hematite phase, the presence of a support material can stabilize FeO and allows a small amount to be formed. Alternatively, for Fe-NP/P25 Fe^{2+} could be present at surface sites of the TiO_2 support or as an iron titanate phase: $FeTiO_3$.

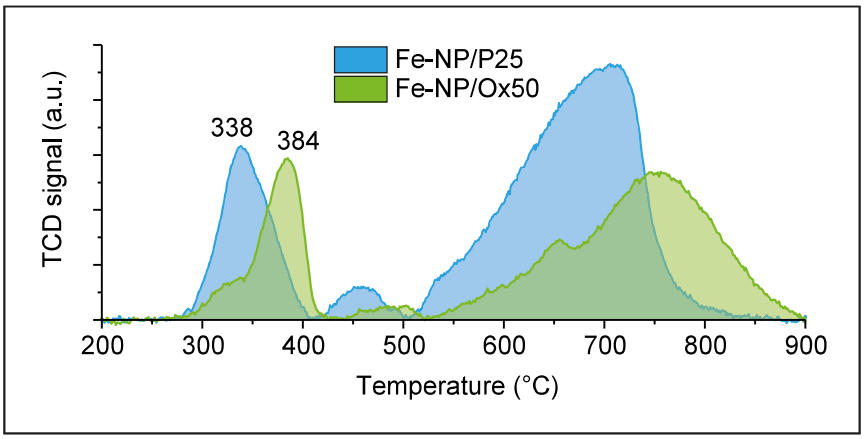

Figure S7: H_2-TPR profile of **Blue)** P25 supported Fe-NP and **Green)** Ox50 supported Fe-NP. Titania supported iron oxide nanoparticles are reduced at slightly lower temperatures than those on silica. The first peak maximum for Fe-NP/P25 occurs around 340°C while the reduction for Fe-NP/Ox50 is delayed to 385°C.

S8 Identical location transmission electron microscopy

HAADF-STEM images of Fe-NP/P25 drop-casted on a SIMPore SN100-A50Q33 chip were made (Figure S8a) and the location of the imaged areas were mapped. Next, the chip was placed in the low pressure setup for a reduction treatment in H_2 at 350°C. The mapped locations were tracked back and imaged after the reduction treatment, see Figure S8b. Unfortunately, the results were not in agreement with the regular reduction experiments. After the reduction in H_2 at 350°C, no particle growth was observed and overlapping particle size distributions were obtained, see Figure S8c. A possible explanation is that the gas flow circumvented the chip and too little H_2 was present to reduce the sample. Another possibility is that SiN in the chip or residual carbon interacted with the catalyst in some way, possibly due to exposure to the electron beam before the reduction.

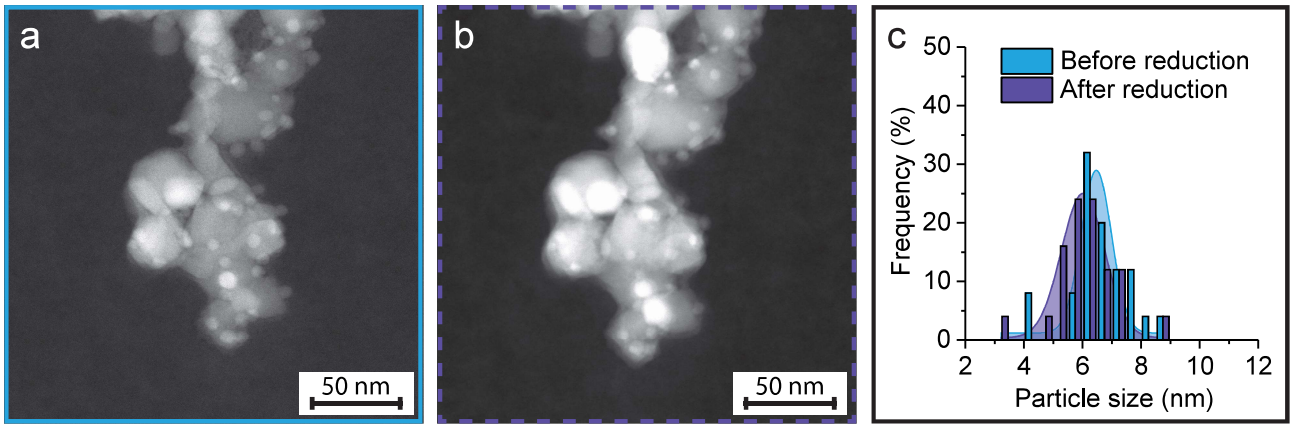

Figure S8: HAADF-STEM image of Fe-NP/P25-1 on a SiN chip **a)** before and **b)** after reduction in H_2 at 350°C and **c)** the corresponding particle size distribution.

S9 Thermodynamic calculations

Figure S9 shows thermodynamic equilibrium composition calculations on the formation metal-support compounds for Fe/TiO_2. HSC Chemistry 7.1 was used to calculate the equilibrium compositions based on the Gibbs free energy. The starting compounds included an excess of H_2(g) or CO(g) of 1000 kmol, 100 kmol TiO_2 (s) and 3 kmol of Fe_3O_4. Aside from the solid Fe, FeOx, TiOx and mixed FexTiOx species, gaseous H_2 and H_2O or CO and CO_2 were included as possible reaction products. In both cases the FeO*TiO_2 phase is thermodynamically stable at temperatures relevant to the reduction experiments.

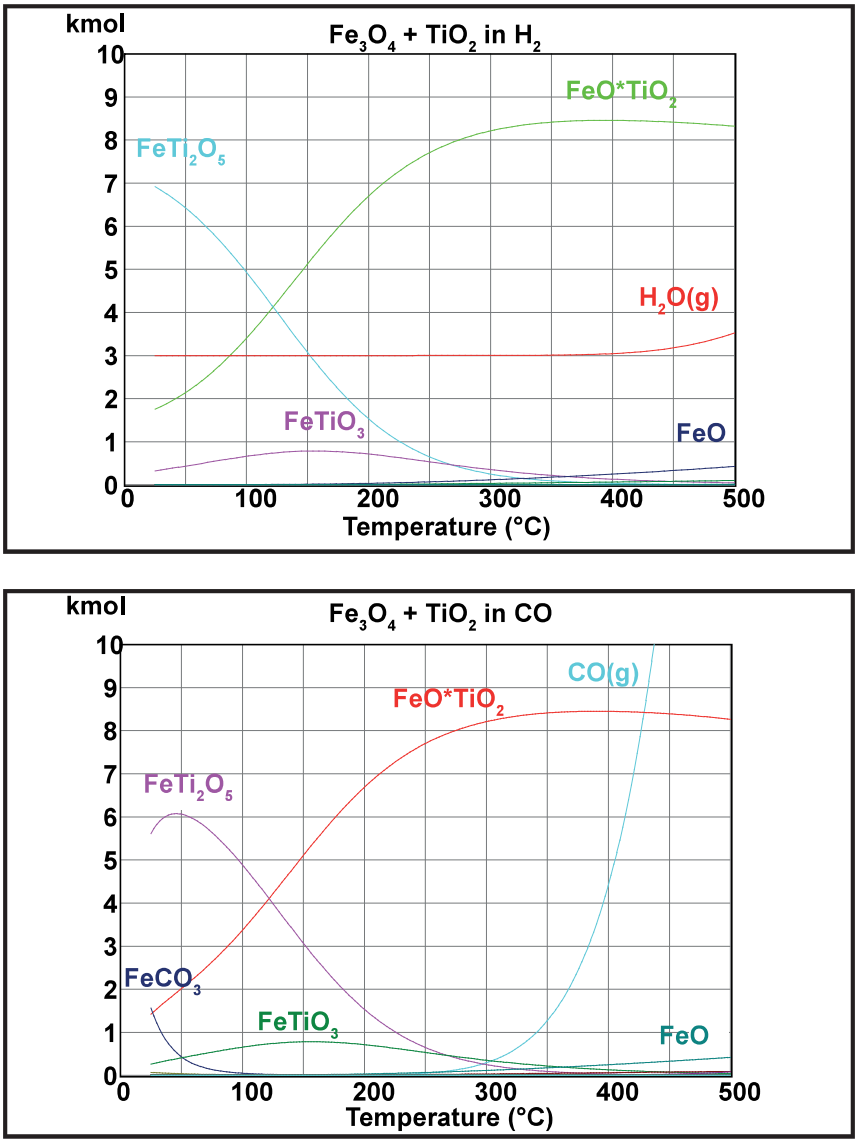

Figure S9: Thermodynamic equilibrium composition calculations for temperatures ranging from 30°C to 500 °C, starting with 3 kmol Fe_3O_4 and 100 kmol TiO_2 with an excess (1000 kmol) of **top)** H_2 or **bottom)** CO.